Check for updates

ChemMedChem

Chemistry Europe
European Chemical Societies Publishing
ChemMedChem

RESEARCH ARTICLE

# New 1,2,3-Triazole Hybrids as Anticancer Agents: Design, Synthesis, Characterization, and In Silico Studies

Alirica I. Suárez[1] | Katiuska E. Chávez[1] | Pablo Martínez[2,3] | José Bubis[2,3] | Zuleyma Blanco[4] | Hegira Ramírez[5] | Jenny Valentina Garmendia[6] | Juan Bautista De Sanctis[6,7] | Soňa Gurská[6,7] | Petr Džubák[6,7,8] | Marián Hajdúch[6,7,8] | Jaime E. Charris[4]

[1]Laboratorio de Productos Naturales, Facultad de Farmacia, Universidad Central de Venezuela, Caracas, Venezuela | [2]Dirección de Salud, Fundación Estudios Avanzados IDEA, Caracas, Venezuela | [3]Departamento de Biología, Universidad Simón Bolívar, Caracas, Venezuela | [4]Laboratorio de Síntesis Orgánica, Facultad de Farmacia, Universidad Central de Venezuela, Caracas, Venezuela | [5]Universidad ECOTEC, Guayaquil, Guayas, Ecuador | [6]Institute of Molecular and Translational Medicine, Faculty of Medicine and Dentistry, Palacky University, Olomouc, Czech Republic | [7]Czech Advanced Technologies and Research Institute (CATRIN), Institute of Molecular and Translational Medicine., Palacky University, Olomouc, Czech Republic | [8]Laboratory of Experimental Medicine., University Hospital Olomouc., Olomouc, Czech Republic

**Correspondence:** Juan Bautista De Sanctis (juanbautista.desanctis@upol.cz) | Jaime E. Charris (jaime.charris@ucv.ve)

**Received:** 6 February 2026 | **Revised:** 13 July 2026 | **Accepted:** 20 July 2026

**Keywords:** click chemistry | molecular docking | natural scaffolds | protein kinase A | quinoline | spheroids | tumor cell lines

## ABSTRACT

Two series of 1,2,3-triazole-based molecules were synthesized. Their physical properties were documented, and cytotoxicity was evaluated against normal lymphocytes, leukemic, adherent, and nontumor cell lines. Compounds **11**, **15**, and **16** were inactive, while compound **17** affected both normal and cancer cells. Compounds **18** and **20** showed activity against BJ and A549 cell lines, with compound **20** being selective for T-cell leukemias and compound **18** moderately affecting B-cell leukemia. Compound **12** specifically affected the HCTp53 KO cell line, while compounds **13** and **14** were selective for U2O2 and HCT116 cell lines, respectively. Compound **14** was highly specific for T-cell leukemia, whereas compound **19** was specific for A549 and moderately specific for B-cell lines. Compound **22** affected all tumor cell lines except A549. The active compound induces apoptosis since it activates caspase 3. Spheroid testing revealed that compounds **13** and **22** specifically affected HCT116 spheroids, while compound **19** affected A549 spheroids. Both in vitro and computational analyses demonstrated that compounds **11**, **12**, and **13** exhibit high affinity for the A Cα subunit of protein kinase A. This suggests a kinase-targeted mechanism of action, providing a structural foundation for future design strategies to optimize the potency of these lead compounds.

## 1 | Introduction

Cancer is defined as a severe disease caused by the uncontrolled growth of cells, leading to tissue destruction and death. It is the second leading cause of death worldwide. Current global statistics for 2022 indicate that there were almost 20 million new cases of cancer and close to 10 million cancer deaths. Demographic predictions suggest that the diagnosis of new cancer cases will reach 35 million by 2050, a 77% increase from the 2022 level [1]. Cancer is a multifaceted disease, and the efficacy of treatment strategies such as surgery, radiotherapy, and chemotherapy is often limited, varying according to the specific stage and type of cancer. Nonetheless, advancements in cancer treatments have occurred over several decades. Contemporary approaches integrate chemotherapeutic regimens with targeted drug delivery, personalized medicine, and immunotherapy, thereby enhancing treatment outcomes. This approach not only improves the efficacy of the enrolled treatment but can also enhance the responsiveness of certain tumors to effective therapeutic targeting in clinical settings [2].

A valuable approach to developing novel drugs involves assembling hybrid molecules with dual modes of action [3–8]. Another

All rights reserved, including rights for text and data mining and training of artificial intelligence technologies or similar technologies.
© 2026 Wiley-VCH GmbH.

approach is the superimposition of structural features responsible for the activity of different chemotherapeutic agents within a single molecular scaffold [9–11]. In this context, we report advances in research on small hybrid molecules as potential candidates against cancer based on in silico and in vitro data reported in the literature to date. Molecular hybridization is a well-established strategy in drug discovery for developing multitarget drug candidates for complex diseases. It consists of the conjugation of two or more pharmacophore units via covalent bonds, resulting in a single molecule that targets multiple pathways and exhibits improved pharmacological and pharmacokinetic profiles compared to the parent pharmacophores used alone or in combination. The hybridization of two active molecules can be achieved in different ways: merged and fused hybrids are obtained by using functional groups initially present on the combination partners, while the introduction of a linker unit, not present in either of the starting pharmacophores, leads to linked hybrids.

Nitrogen-containing heterocyclic compounds are fundamental constituents in many biologically active compounds. The quinoline core and its derivatives represent a significant class of compounds that possess considerable biological importance within the realm of heterocycles. Numerous libraries of quinoline derivatives have been documented, showcasing their notable biological properties. These properties include antibacterial, antifungal, antiviral, antiprotozoal, antimalarial, anti-inflammatory, and anticancer activities [12, 13]. Inspired by the significance of incorporating 1,2,3-triazole functionality into natural scaffolds and in continuation of our search for potent chemotherapeutic agents, we utilized hydroxyl-containing natural bioactive precursors such as eugenol (*Eugenia caryophyllata*), paenol (*Paeonia suffruticosa*), thymol (*Thymus vulgaris*), vanillin (*Vanilla planifolia*), 4-hydroxybenzaldehyde (*Gastrodia elata*, *V. planifolia*), and the compound 3,5-dimethoxy-4-hydroxybenzaldehyde, a synthetic aldehyde, for hybridization purposes. These compounds exhibit versatility and have shown significant efficacy in addressing a wide range of infectious diseases, including bacterial, fungal, protozoal, and viral infections, as well as in anticancer, anti-inflammatory, antituberculosis, antitussive, digestive, carminative, and antispasmodic applications [14–17]. Additionally, the 1,2,3-triazole nucleus is found in several drugs available in the pharmaceutical market or as candidates, such as carboxyamidotriazole, rufinamide, cefatrizine, tazobactam, radezolid, volitinib, seviteronel, molidustat, and TSAO (Figure 1) [18, 19].

The development of cancer treatment strategies targeting protein kinases has been a focus since the 1980s [20]. Protein kinases are one of the most prominent gene families encoded by the human genome. By catalyzing the transfer of the γ-phosphate from ATP to specific target biomolecules, this family of proteins plays a

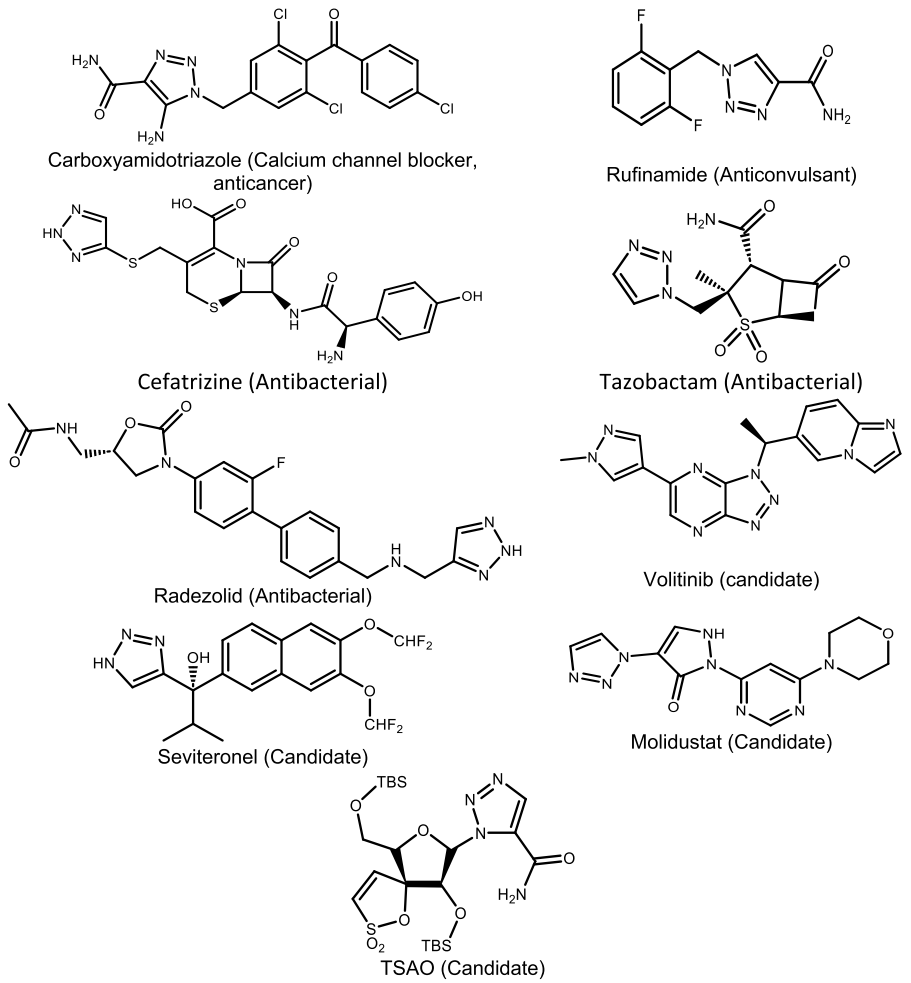


**FIGURE 1** | FDA-approved drugs or drug candidates containing a 1,2,3-triazole scaffold.



18607187, 2026, 15, Downloaded from https://chemistry-europe.onlinelibrary.wiley.com/doi/10.1002/cmdc.70425 by University Palacky, Wiley Online Library on [06/08/2026]. See the Terms and Conditions (https://onlinelibrary.wiley.com/terms-and-conditions) on Wiley Online Library for rules of use; OA articles are governed by the applicable Creative Commons License

crucial regulatory role in almost every biological process and pathway, including cell division, cell death, growth, differentiation, metabolism, and memory [21, 22]. cAMP-dependent protein kinase, also known as protein kinase A (PKA), is considered the archetypal enzyme within this diverse family of proteins, because its structure and catalytic mechanism are very well-studied and provide a model for understanding how all kinases function and are regulated. PKA consists of a complex of two regulatory (R) and two catalytic (C) subunits. Mammals have four R-subunit isoforms (RIα, RIβ, RIIα, and RIIβ) and three catalytic subunit isoforms (Cα, Cβ, and Cγ). The enzyme is inactive in its holoenzyme form; however, when cAMP is present, the holoenzyme dissociates, releasing enzymatically active C subunits for signaling. In normal mammalian cells, PKA is strictly intracellular. Still, cancer cells of various types secrete PKA into the conditioned medium [23–26], making PKA a potential biomarker for cancer detection and a promising therapeutic target [22, 27].

Prompted by these observations and in continuation of our efforts to develop structurally diverse organic scaffolds [28–30], we designed and synthesized a new series of 1,2,3-triazole derivatives from biologically active natural scaffolds. To this end, we employed a well-known, robust, reliable, and efficient copper(I)-catalyzed version of the azide–alkyne cycloaddition reaction, known as the "Click Chemistry" approach developed by Sharpless [31]. The primary motivation for this synthesis was the diverse bioactivities these compounds possess individually, and the study of their anticancer effect after conversion into hybrids linked through the 1,2,3-triazole nucleus.

To elucidate the possible mechanisms of the antiproliferative activities of the investigated compounds, the isoform α of the catalytic subunit of PKA (Cα) was used. A molecular docking study of the apoenzyme structure of the Mus musculus PKA catalytic subunit was performed to analyze the recorded inhibitory effect.

## 2 | Results and Discussion

### 2.1 | Chemistry

The synthesis of 4-aminoquinoline-based precursors involved an initial heating of 4,7-dichloroquinoline with sodium azide in dry DMF to yield **9**. In contrast, a sequence of nucleophilic aromatic substitution with amino ethanol, followed by chlorination and azidation, yielded **10**. Eugenol was obtained by hydrodistillation of cloves purchased at the local market in Caracas, Venezuela. After extraction, the compound was purified by column chromatography on silica gel. Subsequently, eugenol, along with vanillin, paenol, thymol, 4-hydroxybenzaldehyde, and commercially available 3,5-dimethoxy-4-hydroxybenzaldehyde, was propargylated with propargyl bromide and potassium carbonate in dry acetone to yield the corresponding alkyne (**3**–**8**).

Finally, azide (**9**,**10**) and alkyne (**3**–**8**) derivatives underwent Cu(I)-catalyzed [3 + 2] cycloaddition reaction in the presence of a catalytic amount of $CuSO_4 \cdot 5H_2O$ and sodium ascorbate in *tert*-BuOH/$H_2O$ (1:1) mixture for 12 h to yield the title

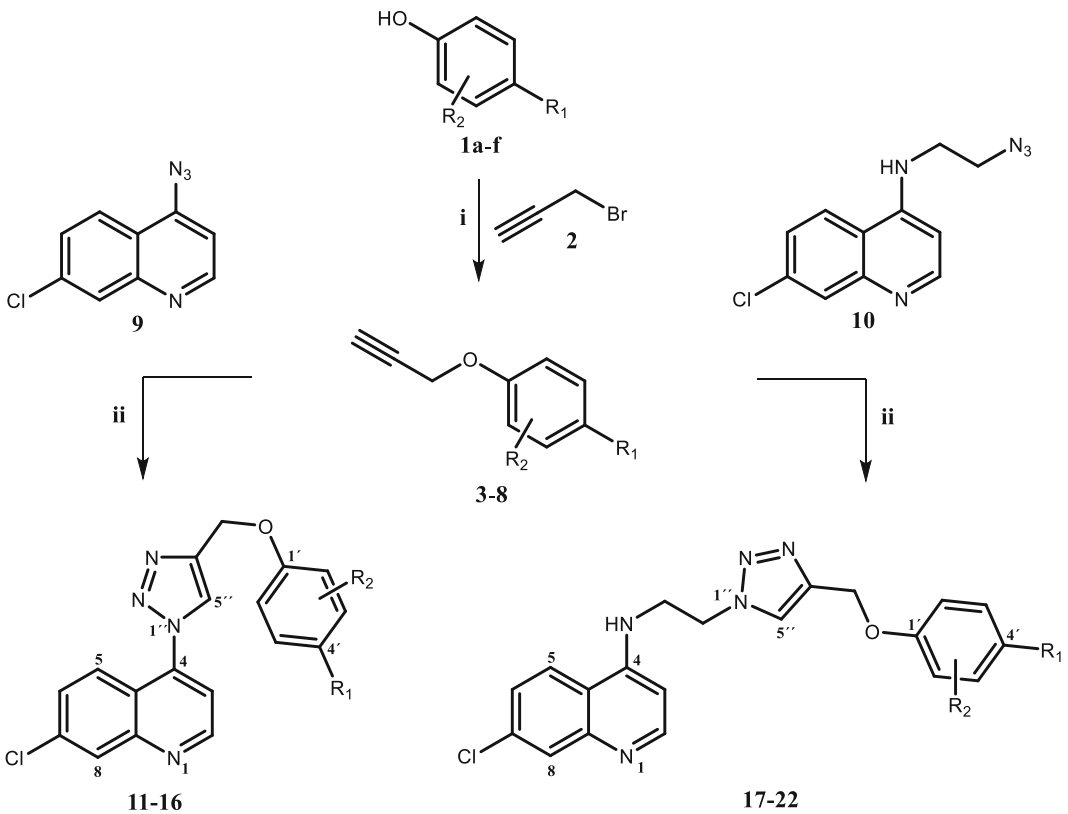


**SCHEME 1** | Synthesis of 1,2,3-triazole derivatives **11**–**22**. (i) $K_2CO_3$, acetone, 60–65 °C. (ii) *tert*-BuOH : $H_2O$ (1:1), sodium ascorbate, $CuSO_4 \cdot 5H_2O$.



18607187, 2026, 15, Downloaded from https://chemistry-europe.onlinelibrary.wiley.com/doi/10.1002/cmdc.70425 by University Palacky, Wiley Online Library on [06/08/2026]. See the Terms and Conditions (https://onlinelibrary.wiley.com/terms-and-conditions) on Wiley Online Library for rules of use; OA articles are governed by the applicable Creative Commons License

compounds (**11**–**22**) (Scheme 1). The crude obtained was purified by silica gel chromatography eluted with dichloromethane (DCM): methanol (9.5:0.5 v/v) to provide the compounds (**11**–**22**) in good to excellent yields. FT-IR, $^{1}H$ and $^{13}C$ NMR, Attached proton test (APT), COSY, HSQC-ME, mass spectrometry, and elemental analysis confirmed the proposed structures.

In the IR spectra of all the compounds (**11**–**22**), the primary evidence for their formation came from the disappearance of the absorption band at 2124 $cm^{-1}$ corresponding to azido functionality indicating that azide had been completely consumed in the reaction and the peak corresponding to alkyne (═C≡CH), which appeared in the range 3227–3292 $cm^{-1}$ was also absent from their spectra. All the synthesized compounds (**11**–**22**) gave characteristic peak of triazole ring in the region 2952–3149 $cm^{-1}$ as broad absorption bands and the band corresponding to the NH group for compounds **17**–**22** in the region 3316–3351 $cm^{-1}$. All the other absorption bands also appeared at the expected regions (Supporting Information).

In the $^{1}H$ NMR spectra, these compounds showed a singlet in the region $\delta$ 7.70–8.24 ppm assigned to H5″ of the triazole ring, thus confirming its formation. The characteristic singlets at δ 5.10–5.59 ppm were also observed for $OCH_2$ protons of triazole derivatives (**11**–**22**). While the triplet corresponding to ≡CH group, which appeared in the region δ 2.49–2.96 ppm was absent from the spectra. In general, the $^{1}H$ NMR spectrum showed the five quinoline protons at 6.42–9.12 ppm and the aliphatic protons at 3.90–1.02 ppm. The triazole ring was further reconfirmed by $^{13}C$ NMR spectral data in which both the carbons of triazole ring appeared in the ranges 120.2–127.3 and $\delta$ 138.3–145.9 ppm. The carbon signals of $OCH_2$ were resonated at δ 62.2–65.2 ppm, while all the other carbons gave peaks at their expected values (Supporting Information).

The mass spectra confirmed the formation of all final products (**11**–**22**). The EI-MS spectra of compounds **12**–**22** displayed molecular ion peaks with very low intensity, and the base peak (100% abundance) corresponded to $C_{12}H_8N_4$; however, for compound **11**, the base peak corresponded to (M - $C_2H_3$). Some of the compounds showed a [M - CHO] peak in the mass spectra, with varying relative intensities (Supporting Information).

## 2.2 | Biology

Cytotoxic activity was assessed using the MTS assay after 72 h of incubation. The $IC_{50}$ value is the concentration of a compound required to kill 50% of cells. Typically, the standard deviation in cytotoxicity assays is up to 20% of the mean. Compounds with an $IC_{50}$ greater than 50 μM are considered inactive. All compounds were inactive against fresh human lymphocytes, with $IC_{50}$ values >50 μM.

Except for compound **11**, the remaining compounds showed some activity against leukemia cells of different origins (Table 1). Compound **12** induced cytotoxicity only in the CCRF-CEM cell line. Compounds **13**, **17**, and **22** were more effective against the leukemic cell lines Raji and Ramos, as shown in Table 1. The differences in $IC_{50}$ values for compounds **13, 17,** and **22**, as measured in cell lines BJ, BJLD (doxorubicin-resistant), MRC-5, and MRC-5LD (doxorubicin-resistant), as well as in

**TABLE 1** | Cytotoxic effect of 7-chloro-(1,2,3-triazol)quinoline derivatives 11–14, 17–22 after 72 h of incubation on leukemic cells.

| | Human leukemia cell lines | | | | | |
|---|---|---|---|---|---|---|
| **No** | **RAJI** | **RAMOS** | **JURKAT E 6.1** | **MOLT-4** | **CCRF-CEM** | **K562** |
| **11** | >50 | >50 | >50 | >50 | >50 | >50 |
| **12** | >50 | >50 | >50 | >50 | 18.7 | >50 |
| **13** | 5.2 ± 0.71 | 2.1 ± 0.33 | 19.6 ± 0.95 | 25.8 ± 1.33 | 18.66 ± 0.88 | 32.2 ± 2.68 |
| **14** | >50 | >50 | 15.8 | 25.6 | 20.15 | >50 |
| **15** | >50 | >50 | >50 | >50 | >50 | >50 |
| **16** | >50 | >50 | >50 | >50 | >50 | >50 |
| **17** | 8.9 ± 0.35 | 5.6 ± 0.42 | 15.9 ± 1.16 | 20.4 ± 2.20 | 11.27 ± 0.74 | 13.78 ± 0.54 |
| **18** | 42.6 ± 3.2 | 35.6 ± 2.26 | >50 | >50 | 37.68 ± 1.88 | >50 |
| **19** | 40.5 ± 2.65 | 38.2 ± 3.31 | >50 | >50 | 36.0 ± 2.76 | >50 |
| **20** | >50 | >50 | 22.5 ± 1.95 | 20.8 ± 1.76 | 25.96 ± 2.38 | >50 |
| **22** | 8.6 ± 0.94 | 3.9 ± 0.74 | 10.6 ± 1.31 | 19.6 ± 1.82 | 17.96 ± 1.60 | 31.19 ± 0.85 |
| **CisPt** | 0.68 ± 0.12 | 0.56 ± 0.08 | 1.1 ± 0.10 | 0.9 ± 0.09 | 4.62 ± 0.15 | 6.98 ± 0.63 |
| **Das** | 19.3 ± 0.32 | 16.8 ± 0.57 | 0.1 ± 0.03 | 1.2 ± 0.13 | 0.03 ± 0.02 | 0.005 ± 0.0.03 |
| **Sora** | 10.5 ± 0.94 | 7.9 ± 0.74 | 6.5 ± 0.32 | 13.5 ± 0.83 | 0.19 ± 0.12 | 5.9 ± 0.45 |
| **Quer** | 34.2 ± 3.22 | 48.9 ± 4.56 | 25.6 ± 4.32 | 35.6 ± 5.83 | 22.3 ± 1.72 | 40.7 ± 5.9 |
| **Fosf** | 2.1 ± 0.15 | 0.3 ± 0.11 | 45.3 ± 2.73 | 44.3 ± 6.15 | 32.3 ± 3.22 | 12.3 ± 2.83 |

*Note:* The table presents the median ± SD of $IC_{50}$ values calculated at μM concentrations for six different assays using Dotmatics software. The standard error of the five assays was 10% or lower for each cell line assayed. When no cytotoxic effect was observed at the highest concentration, the $IC_{50}$ was calculated to be greater than 50 μM. CisPt = cisplatin, Das = dasatinib, Sora = sorafenib, Quer = quercetin, and Fos = Fosfatinib were used as a control. RAJI and RAMOS are derived from B-cell leukemia; JURKAT E6.1, MOLT-4, and CCRF-CEM are derived from T-cell leukemias. K562 is a cell line derived from a patient with Chronic Myelogenous Leukemia.



18607187, 2026, 15, Downloaded from https://chemistry-europe.onlinelibrary.wiley.com/doi/10.1002/cmdc.70425 by University Palacky, Wiley Online Library on [06/08/2026]. See the Terms and Conditions (https://onlinelibrary.wiley.com/terms-and-conditions) on Wiley Online Library for rules of use; OA articles are governed by the applicable Creative Commons License

lymphocytic cell lines Raji and Ramos, were statistically significant ($p < 0.01$). However, these differences were not statistically significant when compared to the JURKAT E 6.1, MOLT-4, CCRF-CEM, and K562 cell lines. Compounds **14** and **20** are specific for T leukemia cell lines, while compounds **18** and **19** affect both B cell lines and the CCRF-CEM cell line. Compounds **15** and **16** did not affect the viability of leukemic cells.

Compounds **13, 14, 17,** and **22** also affected the viability of colon, lung, and osteosarcoma cell lines, with $IC_{50}$ values below 40 μM under standard 2D conditions (Table 2). There were statistically significant differences in $IC_{50}$ values between the lymphocytic leukemia cell lines (Raji and Ramos) and the HCT116 cell line and its p53-knockdown counterpart, HCT116p53−/−parental, as well as the A549 or U2O2 cell lines. The results obtained with compounds **13** and **22** differ significantly between HCT and U2OS cell lines and between the normal BJ, BJLD, MRC-5, and MRC-5LD cell lines ($p < 0.01$). However, compound **17** did not show a statistically significant difference in the cell lines tested (Tables 2 and 3). Compounds **17–20** were active against the lung adenocarcinoma cell line A549. No specificity was detected for compound **17**. Compounds **18**, **19**, and **20** were selective for the A549 cell line (Table 2); however, their effects differed significantly ($p < 0.01$) across the other affected cell lines. Compound **19** had the highest selectivity for the A549 cell line; it did not affect normal fibroblasts and induced moderate cytotoxicity against leukemia cell lines. This compound is highly specific. Compound **18** shows results similar to those of compound **20**; both affect BJ cell lines. On the other hand, compound **20** is specific for T-cell leukemias, whereas compound **18** moderately affects B-cell lines and one T-lymphocyte cell line; it is less specific. Derivatives **11**, **12**, **14**, **18**, **19,** and **20** were inactive against the human osteosarcoma cell line U2O2. Structures **15** and **16** did not affect the viability of any tumor cell lines (Tables 1 and 2) and nontumoral cell lines (Table 3).

The effects of the compounds and controls on the viability of spheroids from HCT116, HCT116 TP53−/−, and A549 are represented in (Tables 4 and 5). Even though the $IC_{50}$ could not be reached at the tested concentrations, differences between HCT116 and HCT116 TP53−/− were evident in the A549 cell line. The compounds did not affect spheroids generated from the fibroblast cell lines BJ or MRC5 ($IC_{50} > 50$ μM). Compound **19**, as in 2D cell cultures, affected A549 spheroids, although the effect was observed only at the highest concentration. Compounds **13** and **22,** which had moderate effects in 2D cultures of HCT116 cells, also showed similar effects in spheroid cultures.

In another set of experiments, compounds **13**, **19,** and **22** did not affect U2OS spheroids ($p > 50$ μM).

### *2.2.1 | Apoptosis Quantification Using Cleaved Caspase-3 (Asp175) ELISA Assay*

The results in Figure 2 confirm the compounds' ability to induce apoptosis in the different cell lines. It is clear that the process does not involve any other mechanism.

### *2.2.2 | Inhibition of PKA*

Mouse PKA Cα-subunit was expressed in bacteria and purified to homogeneity by column chromatography through CM

**TABLE 2** | Cytotoxic effect of 7-chloro-(1,2,3-triazol)quinoline derivatives 11–14, 17–20 after 72 h of incubation with different human fibroblast cultures.

| | Human tumors 2D | | | |
|---|---|---|---|---|
| **No** | **HCT116** | **HCT116p53−/−** | **A549** | **U2O2** |
| **11** | >50 | >50 | >50 | >50 |
| **12** | >50 | 36.23 ± 1.23 | >50 | >50 |
| **13** | 26.15 ± 2.21 | 21.34 ± 1.88 | >50 | 34.27 ± 1.98 |
| **14** | 33.83 ± 1.74 | 36.85 ± 2.33 | >50 | >50 |
| **15** | >50 | >50 | >50 | >50 |
| **16** | >50 | >50 | >50 | >50 |
| **17** | 24.58 ± 2.12 | 22.37 ± 1.11 | 28.53 ± 1.33 | 22.2 ± 2.56 |
| **18** | >50 | >50 | 25.82 ± 1.52 | >50 |
| **19** | >50 | >50 | 12.39 ± 1.16 | >50 |
| **20** | >50 | >50 | 26.25 ± 2.13 | >50 |
| **22** | 35.57 ± 3.17 | 33.85 ± 4.92 | >50 | 31.34 ± 3.45 |
| **CisPt** | 12.52 ± 0.6 | 8.34 ± 0.35 | 9.51 ± 1.72 | 9.56 ± 0.85 |
| **Das** | 0.9 ± 0.3 | 3.1 ± 0.52 | 2.6 ± 2.1 | 2.9 ± 1.8 |
| **Sora** | 15.8 ± 0.91 | 9.8 ± 0.16 | 11.6 ± 1.30 | 10.8 ± 0.63 |
| **Quer** | 39.5 ± 2.32 | >50 | 15.3 ± 1.24 | >50 |
| **Fosf** | 35.2 ± 1.3 | >50 | >50 | 21.2 ± 3.9 |

*Note:* The table presents the median ± SD of $IC_{50}$ values calculated at μM concentrations for six different assays using Dotmatics software. The standard error of the five assays was 10% or lower for each cell line assayed. When no cytotoxic effect was observed at the highest concentration tested, the $IC_{50}$ was calculated to be greater than 50 μM. CisPt = cisplatin, Das = dasatinib, Sora = sorafenib, Quer = quercetin, and Fos = Fosfatinib were used as a control. HCT116 cell lines are epithelial cells from colon carcinoma, A549 are apithelial cells derived from lung cancer, and U2O2 are cells derived from osteosarcoma.



18607187, 2026, 15, Downloaded from https://chemistry-europe.onlinelibrary.wiley.com/doi/10.1002/cmdc.70425 by University Palacky, Wiley Online Library on [06/08/2026]. See the Terms and Conditions (https://onlinelibrary.wiley.com/terms-and-conditions) on Wiley Online Library for rules of use; OA articles are governed by the applicable Creative Commons License

**TABLE 3** | Cytotoxic effect of 7-chloro-(1,2,3-triazol)quinoline derivatives 11–14, 17–22 after 72 h of incubation with different human fibroblast cultures.

| | Human fibroblast | | | |
|---|---|---|---|---|
| **No** | **BJ** | **BJ LD** | **MRC-5** | **MRC-5 LD** |
| **11** | >50 | >50 | >50 | >50 |
| **12** | >50 | >50 | >50 | >50 |
| **13** | >50 | >50 | >50 | >50 |
| **14** | >50 | >50 | >50 | >50 |
| **15** | >50 | >50 | >50 | >50 |
| **16** | >50 | >50 | >50 | >50 |
| **17** | 27.6 ± 1.76 | 27.01 ± 1.92 | 21.41 ± 2.35 | 22.3 ± 1.78 |
| **18** | 31.79 ± 1.33 | 17.43 ± 1.22 | >50 | >50 |
| **19** | >50 | >50 | >50 | >50 |
| **20** | 30.26 ± 1.05 | 8.43 ± 0.77 | >50 | >50 |
| **22** | >50 | >50 | >50 | >50 |
| **CisPt** | 9.5 ± 0.31 | 17.8 ± 0.83 | 3.98 ± 0.35 | 23.5 ± 0.43 |
| **Das** | >50 | >50 | 8.6 ± 0.61 | 15.8 ± 0.52 |
| **Sofer** | >50 | >50 | 47.8 ± 2.21 | >50 |
| **Quer** | >50 | >50 | >50 | >50 |
| **Fosf** | 48.9 ± 2.72 | >50 | >50 | >50 |

*Note:* The table presents the median $IC_{50}$ values calculated at μM concentrations for five different assays using Dotmatics software. The standard error of the five assays was 10% or lower for each cell line assayed. When no cytotoxic effect was observed at the highest concentration tested, the $IC_{50}$ was calculated to be greater than 50 μM. CisPt = cisplatin, Das = dasatinib, Sora = soferamid, Quer = quercetin, and Fos = Fosfatinib were used as a control. BJ cells are human fibroblasts isolated from the foreskin of a healthy newborn male. The MRC-5 cell line is derived from normal lung tissue of a 14-week-old Caucasian male fetus. The BJ-LD and MRC-5 LD cell lines are doxorubicin-resistant.

**TABLE 4** | Effect of the compounds on spheroids. Percent of ATP released.

| | HCT116 | | | HCT116 TP53−/− | | | A549 | | |
|---|---|---|---|---|---|---|---|---|---|
| **No** | **10, μM** | **25, μM** | **50, μM** | **10, μM** | **25, μM** | **50, μM** | **10, μM** | **25, μM** | **50, μM** |
| **13** | 8.3 ± 1.6 | 20.0 ± 3.8 | 44.9 ± 2.2 | 12.3 ± 2.5 | 24.5 ± 3.6 | 31.2 ± 1.3 | 0 | 0 | 0 |
| **19** | 0 | 0 | 0 | 0 | 0 | 0 | 0 | 0 | 10.3 ± 0.9 |
| **22** | 8.5 ± 1.3 | 19.8 ± 2.2 | 35.5 ± 4.5 | 6.3 ± 1.5 | 15.5 ± 1.3 | 30.8 ± 2.7 | 0 | 0 | 0 |

*Note:* The values represent the percentage of ATP released from spheroids after 72 h of treatment, relative to nontreated controls. The $IC_{50}$ for cisplatin was 14.8, 43.5, and 49.1 μM for the cell lines HCT116, HCT116 TP53−/−, and A549, respectively.

**TABLE 5** | Controls of the assay $IC_{50}$ in μM.

| | HCT116 | HCT116 TP53−/− | A549 |
|---|---|---|---|
| **CisPt** | 14.8 ± 1.2 | 43.5 ± 3.44 | 49.1 ± 5.8 |
| **Das** | 29.5 ± 3.9 | 47.6 ± 4.12 | >50 |
| **Sora** | 15.8 ± 1.3 | 22.3 ± 1.8 | 11.2 ± 0.3 |
| **Quer** | >50 | >50 | >50 |
| **Fosf** | >50 | >50 | >50 |

*Note:* The $IC_{50}$ for cisplatin was 14.8 ± 1.2, 43.5 ± 3.44, and 49.1 ± 5.8 μM for the cell lines HCT116, HCT116 TP53−/−, and A549, respectively.

Sepharose. The elution profile of the protein after applying a linear salt gradient is illustrated in Figure 3A. The recombinant Cα subunit corresponded to a polypeptide band migrating with an apparent molecular mass of ~40 kDa on sodium dodecyl sulfate-polyacrylamide gel electrophoresis (SDS-PAGE) (Figure 3B).

Kinase activity of the purified protein was determined using an electrophoretic gel-shift nonradioactive assay. The phosphorylated and nonphosphorylated fluorescently labeled kemptide bands were easily separated by electrophoresis on an agarose gel (Figure 3C).

Initially, the enzymatic activity of the purified PKA Cα-subunit was evaluated following incubation with a fixed concentration of the synthesized compounds (10 μM). The table in Figure 4A qualitatively summarizes the compounds' effects on the protein's ATP: phosphotransferase activity. Compounds **11** and **13** possessed the highest inhibitory effect (+++), whereas compound **12** showed an intermediate inhibitory effect (++, Figure 4A. Additionally, compounds **14**, **15**, **20**, and **21** had little inhibitory effect (+, Figure 4A), whereas the remaining compounds (**17**, **18**, **19**, and **22**) had no effect (−, Figure 4A).

Here, we focus on compounds **11**, **12**, **13**, and **14**, as they share a similar quinoline–triazole core. Figure 4B illustrates the



18607187, 2026, 15, Downloaded from https://chemistry-europe.onlinelibrary.wiley.com/doi/10.1002/cmdc.70425 by University Palacky, Wiley Online Library on [06/08/2026]. See the Terms and Conditions (https://onlinelibrary.wiley.com/terms-and-conditions) on Wiley Online Library for rules of use; OA articles are governed by the applicable Creative Commons License

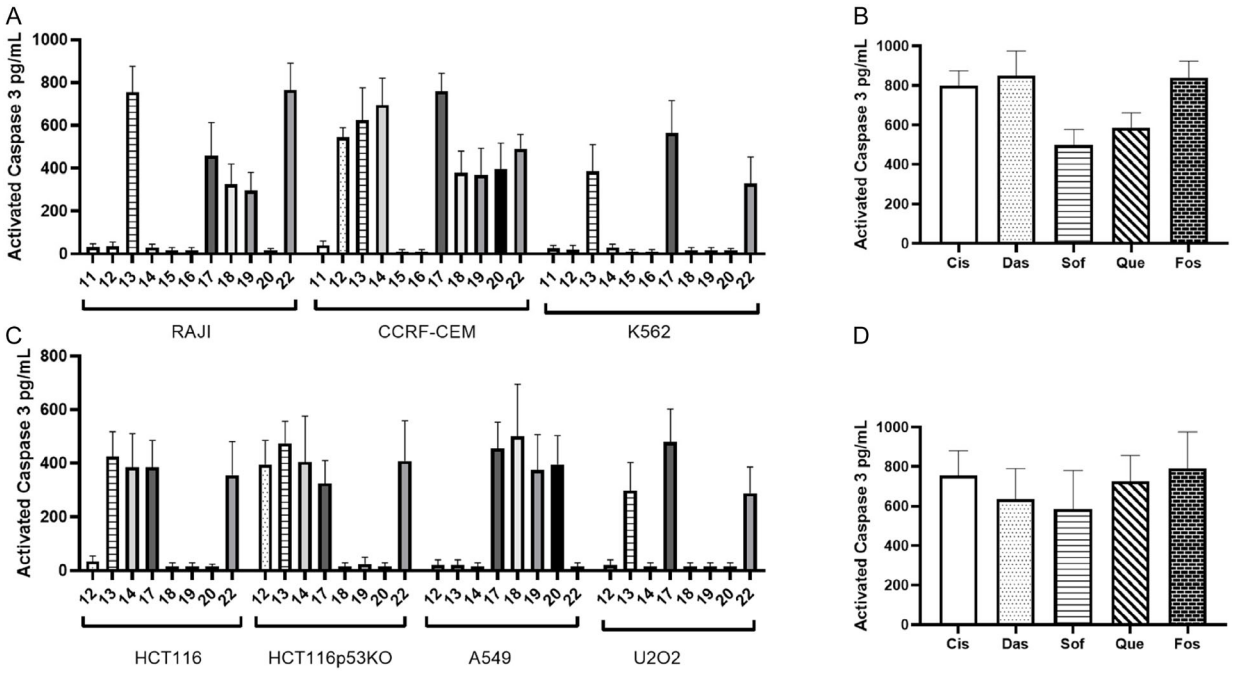


**FIGURE 2** | Illustrates the effect of the different compounds on the activation of caspase 3, a critical marker in apoptosis, using the (Asp175) ELISA assay. (A) The effect of all the compounds ($n = 6$) on the (B) cell leukemia cell line Raji, the T cell CCRF-CEM, and the K562 cell line. The concentration of the compound was 25 μM. The treatment was for 12 h. (B) The positive controls at the $IC_{50}$ concentrations expressed in Table 2. (C) The effect of 25 μM of each compound on adherent tumor cell lines ($n = 6$). The compounds **11**, **15**, and **16** were not represented. (D) The positive controls at the $IC_{50}$ calculated. The treatment was for 12 h.

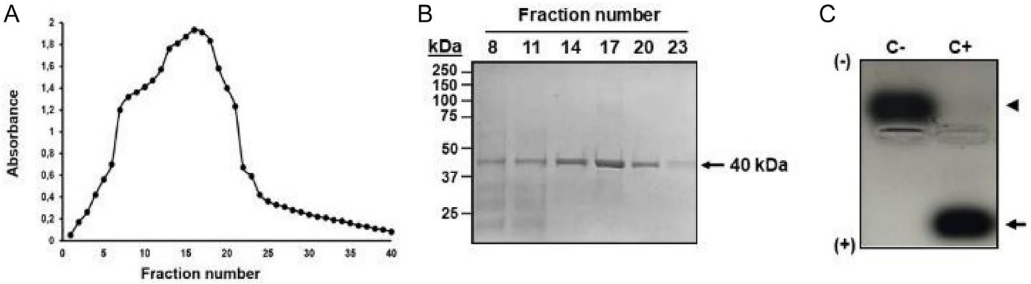


**FIGURE 3** | Purification of the recombinant *M. musculus* PKA Cα-subunit. (A) Mouse PKA Cα-subunit was purified to homogeneity on a CM Sepharose column. The elution profile was monitored at 280 nm. (B) The resulting fractions were examined by SDS-PAGE, and the various lanes illustrate the polypeptide content of the corresponding column fractions. The arrow indicates the migration and apparent molecular mass of the purified protein. (C) Kinase activity was measured using an electrophoretic agarose gel-shift assay using fluorescently labeled kemptide. Shown is the result obtained when the purified PKA catalytic subunit was included in the reaction mixture (C+). The reaction mixture without any added enzyme was used as a negative control (C−). The arrowhead and arrow indicate the nonphosphorylated and phosphorylated peptide, respectively. Phosphorylated kemptide migrated toward the positive electrode (+), while nonphosphorylated kemptide migrated toward the negative electrode (−).

inhibition obtained on the enzymatic activity of the PKA Cα-subunit when the protein was incubated with 10 μM of **11**, **12**, **13,** and **14**. The electrophoretic gel-shift kinase assay clearly showed that **11** and **13** were potent inhibitors, whereas **12** and **14** were intermediate and low inhibitors, respectively (Figure 4B).

Based on these preliminary findings, increasing concentrations of **11** and **13** (0 to 10 μM) were added to the recombinant PKA Cα-subunit, and its remaining kinase activity was measured. After densitometric quantitation, dose-dependent inhibition of the enzyme was detected (Figure 4C), with $IC_{50}$ values of $2.05 \pm 1.58$ and $6.80 \pm 2.35$ μM for **11** and **13**, respectively. The order of effectiveness of the four compounds as PKA Cα-subunit inhibitors was **11** > **13** > **12** >> **14**.

To evaluate whether MgATP protected against the inhibition of the enzyme by these reagents, the PKA Cα subunit was preincubated with the nucleotide before the addition of the compounds to the protein. Interestingly, preincubation of the protein with MgATP completely protected against the inhibitory effect of all four compounds (data not shown). These results strongly suggest that these reagents bind to the enzyme's MgATP-binding pocket.

The determination of the crystal structure of the PKA Cα subunit [32, 33] showed that the protein core is bilobal. Although the



18607187, 2026, 15, Downloaded from https://chemistry-europe.onlinelibrary.wiley.com/doi/10.1002/cmdc.70425 by University Palacky, Wiley Online Library on [06/08/2026]. See the Terms and Conditions (https://onlinelibrary.wiley.com/terms-and-conditions) on Wiley Online Library for rules of use; OA articles are governed by the applicable Creative Commons License

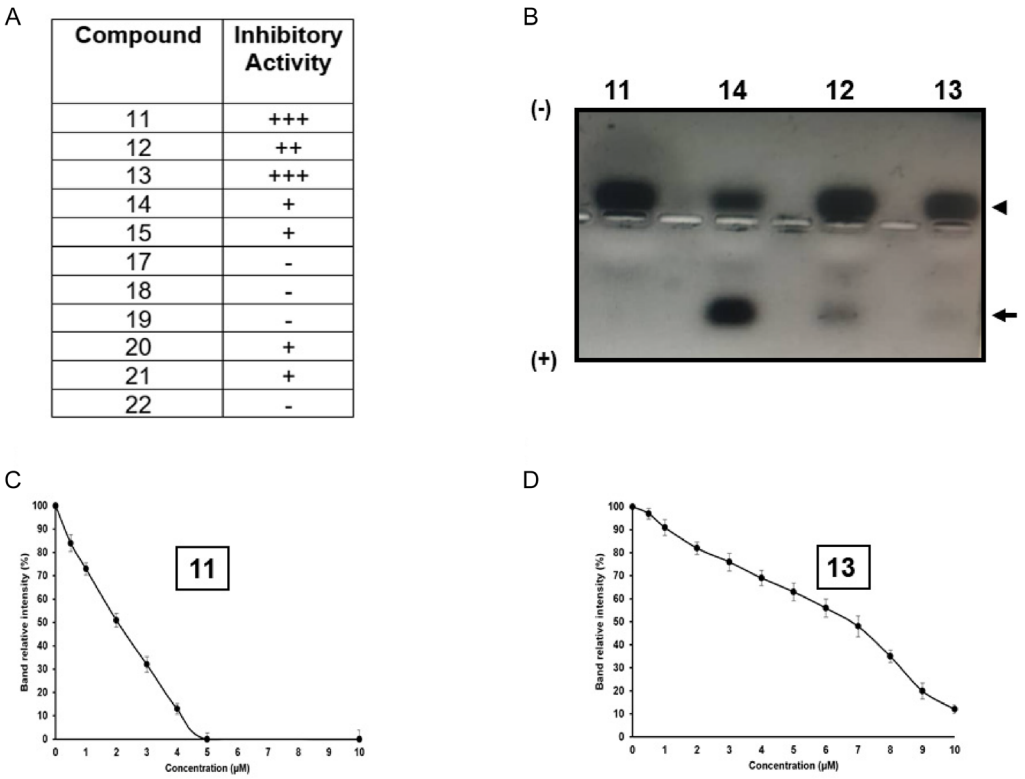


**FIGURE 4** | Effect of the synthesized Click compounds on the enzymatic activity of the PKA Cα-subunit. (A) Kinase activity of the purified PKA Cα-subunit following incubation with 10 μM of the new series of 1,2,3-triazole hybrids. Positive inhibitory reactions were qualitatively classified with one cross (+), two crosses (++), or three crosses (+++). No inhibitory effect was indicated by a negative sign (−). (B) Inhibition of the enzymatic activity of the PKA Cα-subunit after incubation with 10 μM of **11**, **12**, **13,** and **14**. Reaction mixtures were separated by electrophoresis on a 1% agarose gel, and the gel was visualized under a phototransilluminator using UV light. The arrowhead and arrow indicate the nonphosphorylated and phosphorylated fluorescently labeled kemptide, respectively. (C) and (D) Dose-dependent inhibition of the PKA Cα-subunit following addition of increasing concentrations of compounds **11** and **13**, respectively. The relative intensity of the phosphorylated kemptide band (%) was plotted against the concentration of each compound.

ATP-binding site is mainly situated in the N-terminal lobe, the ATP-binding pocket spans both lobes, since the nucleotide molecule is located in the cleft between the two domains. Figure 5 shows the residues of the PKA Cα subunit that participate in ATP binding on the basis of the low- and room-temperature 3D X-ray structures of ternary complexes solved in the presence of high $Mg^{2+}$, ATP, and the inhibitory peptide IP20 (sequence = TTYADFIASGRTGRRNAIHD), a 20-residue peptide derived from the heat-stable inhibitor PKIα [34]. The ATP-binding site shows the intricate network of hydrogen bonds and electrostatic interactions that buries the nucleotide within the protein. Amino acids in the glycine-rich loop (G-loop, residues 40–64) embrace the adenine ring of the molecule and help to secure it at the base of the cleft as well as to position the γ-phosphate for transfer to a protein substrate. Various residues, such as Leu 49, Val 57, Ala 70, Met 120, Val 123, Leu 173, and Thr 183 (among others), have been identified to interact with the nucleotide base and generate an expanded hydrophobic shell that surrounds the ATP and defines the entropy-driven allostery that drives the phosphoryl transfer mechanism. Other crucial residues are Lys 72, which plays a fundamental role in ATP binding, enzyme stability, and catalytic activity, and Asp 184 in the DFG motif, which, besides playing an essential role in enzyme catalysis and active site structure, binds to the second metal ion in the ATP complex (not shown in Figure 5).

Comparative analysis of the molecular docking results revealed distinct binding modes among compounds **11**–**14**. Compounds **11**–**13** (Figure 6A–C) interacted predominantly with residues that constitute the canonical ATP-binding pocket of PKA, including Lys72, Leu49, Phe54, Leu74, Met120, and Val57, which are well recognized as key contributors to kinase inhibitor binding. Some of the primary residues participating in the binding of ligands **11**–**13** comprise amino acids in the G-loop, like L49, F54, G55, and V57 (Figure 6A–C). Since these residues are known to be involved in the correct positioning of the ATP phosphate groups, our docking results denote conserved interaction hotspots within the protein ATP-binding site. The extensive network of hydrophobic, π-mediated, and electrostatic interactions established with these conserved residues is likely to promote stable ligand accommodation within the active site, thereby favoring PKA inhibition. In contrast, compound **14** (Figure 6D) exhibited a notably different interaction profile, with its binding mode shifted toward residues Asp175, Glu121, and Tyr306, suggesting an altered orientation of the ligand within the ATP-binding pocket. This change in binding orientation, together with the absence of additional favorable interactions with the canonical ATP-binding residues and the presence of an unfavorable acceptor–acceptor interaction involving Asp175, may reduce ligand–protein complementarity and compromise complex stability. More specifically, compound **11** exhibited the most



18607187, 2026, 15, Downloaded from https://chemistry-europe.onlinelibrary.wiley.com/doi/10.1002/cmdc.70425 by University Palacky, Wiley Online Library on [06/08/2026]. See the Terms and Conditions (https://onlinelibrary.wiley.com/terms-and-conditions) on Wiley Online Library for rules of use; OA articles are governed by the applicable Creative Commons License

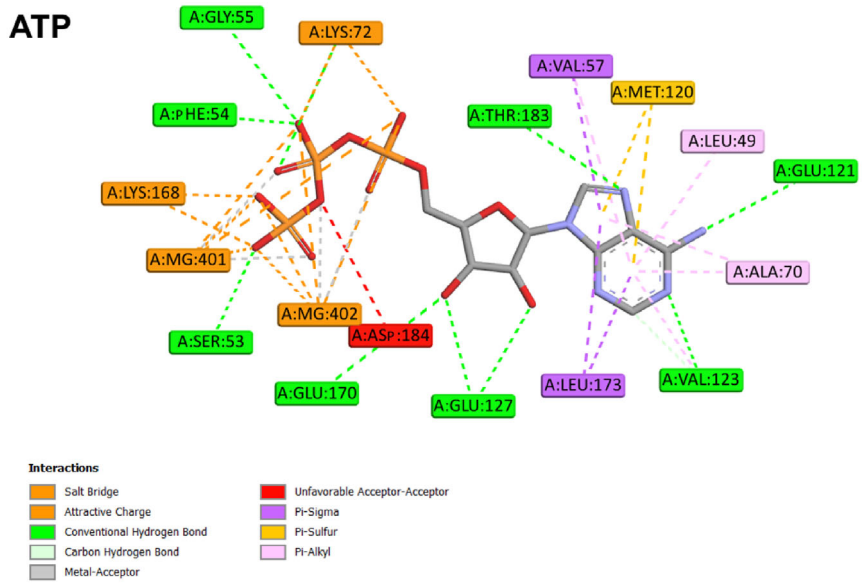


**FIGURE 5** | A close-up view of the ATP binding site in the X-ray structure of the PKA Cα subunit solved with high $Mg^{2+}$, ATP, and IP20 (PDB code: 4DH3). The adenine is located in a hydrophobic pocket, and hydrogen bonds stabilize the ribose. The phosphates of ATP are aligned for catalysis by interactions with the main chain nitrogens of the glycine-rich loop, by interactions with Lys 72, and by interactions with $Mg^{2+}$ ions (not shown). Residues are denoted by using the three-letter abbreviations for the standard amino acids with their corresponding position in the sequence.

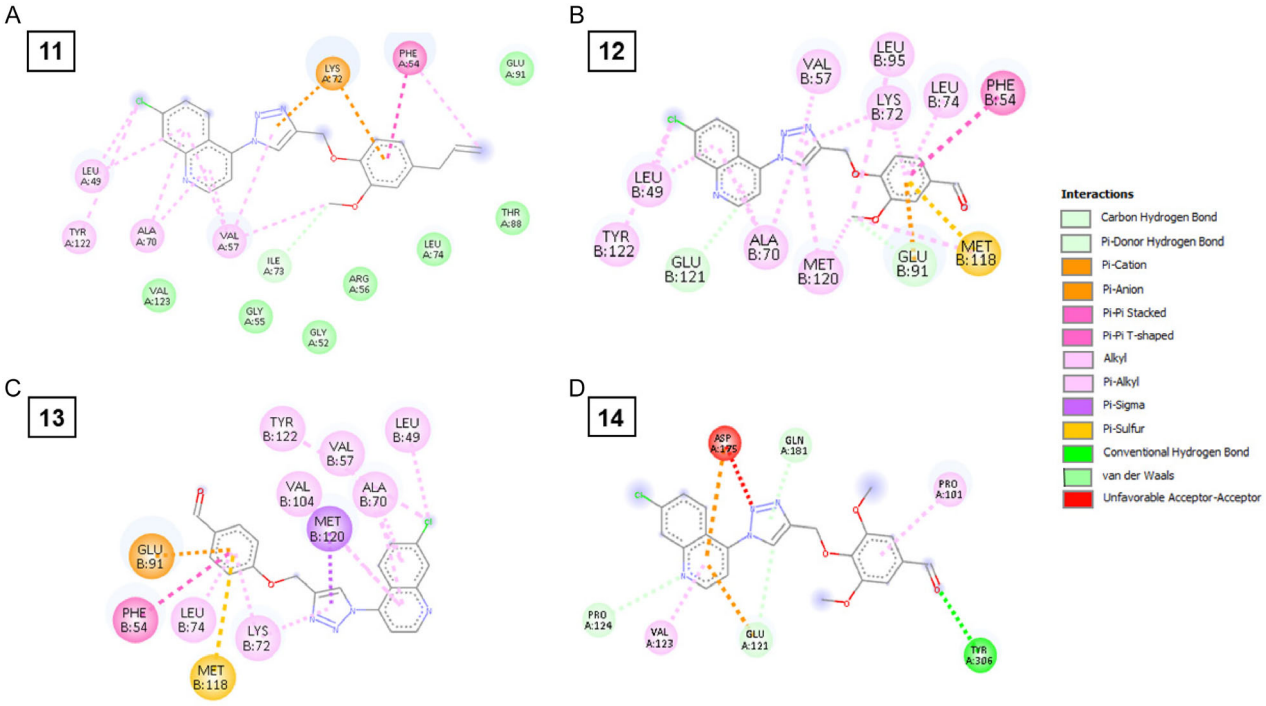


**FIGURE 6** | Molecular docking of compounds **11**, **12**, **13**, and **14** to the PKA Cα-subunit**.** Shown are computational predictions of how the four Click compounds, **11** (A), **12** (B), **13** (C), and **14** (D), fit into the ATP binding site of the PKA Cα-subunit. Shown are 2D molecular interactions of each of the four compounds with critical residues that participate in the binding of ATP in the protein. Residues are denoted by using the three-letter abbreviations for the standard amino acids with their corresponding position in the sequence. Interactions were displayed as color-coded dashed lines. Docking scores were −8.4, −8.0, −8.2, and −7.2 for compounds **11**, **12**, **13**, and **14**, respectively. Each score represents the binding affinity or stability of the protein–compound complex, estimated by minimizing the system's free energy.

favorable docking score (−8.4), suggesting a strong affinity for the PKA catalytic subunit. This result is consistent with the highest inhibition profile obtained for compound **11** (Figure 4). In contrast, compound **14**, bearing a 3,4-dimethoxy-substituted aromatic ring, exhibited the highest docking score (−7.2), and the weakest inhibitory activity against PKA (Figure 4), despite forming several hydrophobic and π-mediated interactions with the ATP molecule. Molecular docking analysis of compound



18607187, 2026, 15, Downloaded from https://chemistry-europe.onlinelibrary.wiley.com/doi/10.1002/cmdc.70425 by University Palacky, Wiley Online Library on [06/08/2026]. See the Terms and Conditions (https://onlinelibrary.wiley.com/terms-and-conditions) on Wiley Online Library for rules of use; OA articles are governed by the applicable Creative Commons License

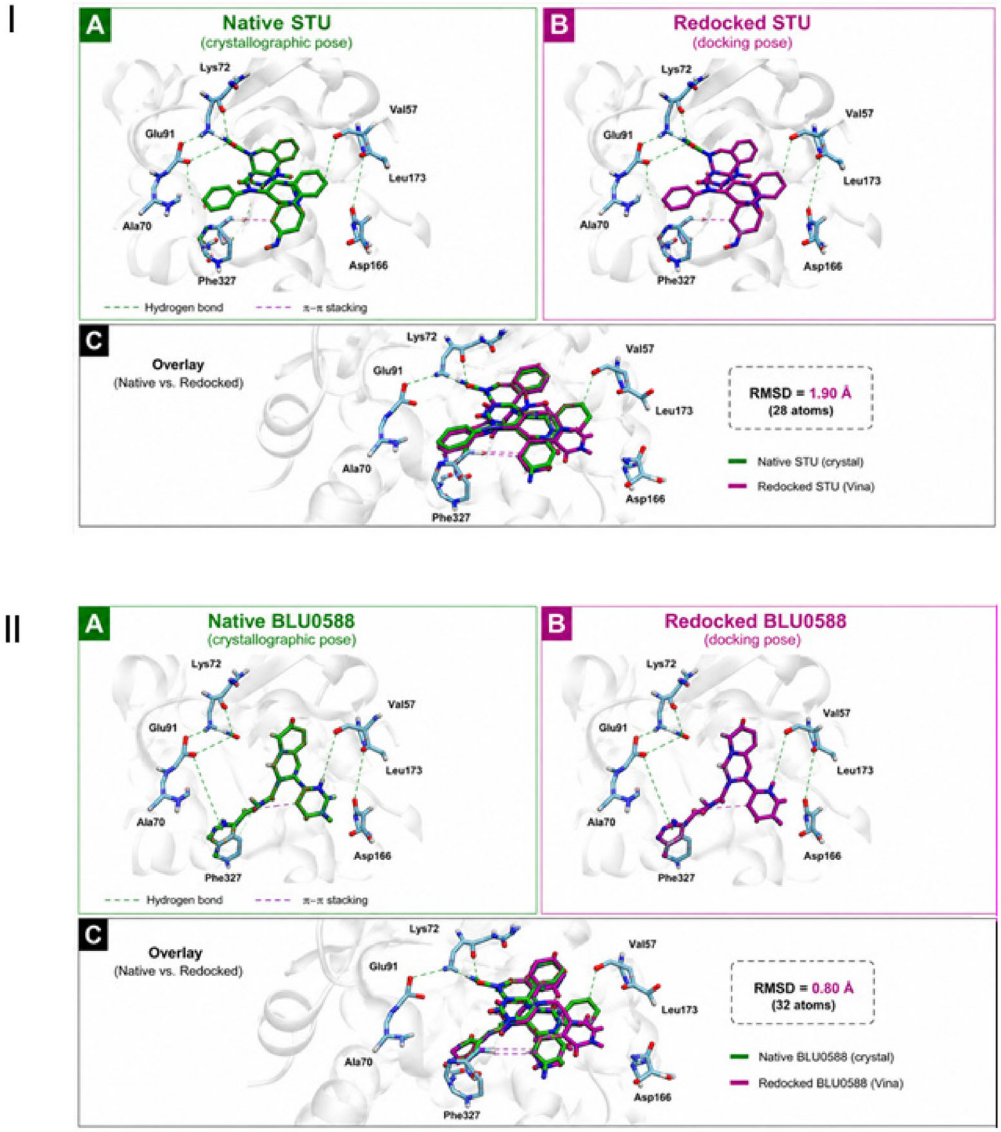


**FIGURE 7** | Validation of the molecular docking protocol by redocking two cocrystallized inhibitors of the PKA Cα-subunit, staurosporine (STU) from PDB ID: 1STC and BLU0588 from PDB ID: 9PC1. Panel I: (A) crystallographic binding pose of STU within the PKA Cα-subunit active site; (B) binding pose of STU obtained by redocking using AutoDock Vina; and (C) superposition of the crystallographic (green) and redocked (magenta) ligand conformations, showing an RMSD of 1.9 Å (28 heavy atoms). Panel II: (A) crystallographic binding pose of BLU0588; (B) binding pose obtained by redocking using AutoDock Vina; and (C) superposition of the crystallographic (green) and redocked (magenta) ligand conformations, showing an RMSD of 0.80 Å (32 heavy atoms).

**14** revealed π-anion interactions with Asp175 and Glu121, π-alkyl contacts with Val123 and Pro101, and a conventional hydrogen bond with Tyr306. However, an unfavorable acceptor–acceptor interaction involving Asp175 was also observed, which might compromise the stability of the ligand–protein complex. Notably, the introduction of a second methoxy substituent increases the steric demand of the aromatic ring, which may induce a less favorable orientation of the aromatic moiety, impairing the optimal accommodation of the quinoline–triazole scaffold within the active site, a phenomenon frequently associated with reduced ligand–protein complementarity and binding affinity [35]. Consequently, the absence of additional stabilizing interactions, together with the unfavorable electrostatic contact, may contribute to the reduced binding affinity predicted by molecular docking and is consistent with the experimentally observed weak PKA inhibitory activity of compound **14**. Summarizing, docking studies have confirmed that residues involved in the MgATP-binding site of the PKA Cα-subunit also participate in the binding of the synthesized Click compounds to the protein (Figure 6). The presence of significant interactions suggests that these ligands may stabilize the protein in a state that hinders ATP binding or catalytic activity.

The reliability of the molecular docking protocol was evaluated through independent redocking of two cocrystallized PKA inhibitors: staurosporine (STU) (PDB ID: 1STC [36]) and BLU0588 (PDB ID: 9PC1) [37]. As shown in Figure 7, Panel I, the redocked STU pose accurately reproduced the crystallographic binding orientation within the ATP-binding pocket, maintaining the key interactions observed experimentally. Superposition of the



18607187, 2026, 15, Downloaded from https://chemistry-europe.onlinelibrary.wiley.com/doi/10.1002/cmdc.70425 by University Palacky, Wiley Online Library on [06/08/2026]. See the Terms and Conditions (https://onlinelibrary.wiley.com/terms-and-conditions) on Wiley Online Library for rules of use; OA articles are governed by the applicable Creative Commons License

crystallographic and predicted poses yielded an root–mean-square deviation (RMSD) of 1.9 Å for 28 heavy atoms, indicating successful reproduction of the experimental binding mode. Moreover, redocking of BLU0588 resulted in excellent agreement with its crystallographic conformation (Figure 7, Panel II). The predicted pose maintained the overall orientation and interaction pattern within the active site and exhibited an RMSD of 0.80 Å for 32 heavy atoms, demonstrating an even closer correspondence between the experimental and the predicted structures. The docking protocol used for compounds **11**–**14** appeared to be suitable, since RMSD values below 2.0 Å are generally considered indicative of successful reproduction of the experimental binding mode [38].

Quinolines have been identified as a valuable scaffold for the development of kinase inhibitors with therapeutic potential. One example is the 3H-pyrazolo[4,3–f]quinoline moiety, a privileged kinase inhibitor core with potent activity against acute myeloid leukemia (AML) cell lines [39]. The four compounds **11**, **12**, **13**, and **14** contain the same quinoline–triazole core as the 3H-pyrazolo[4,3–f]quinoline moiety, which may disrupt the hydrogen-bonding interactions in the hinge region of PKA. Therefore, the focus is on the different aryl substituents to explain the observed variations in inhibitory activity. For example, compound **11**, identified as the most effective inhibitor, features a para-allyl substituent. This substituent likely provides an extended hydrophobic moiety that may integrate into the lipophilic groove located beneath the glycine-rich loop. This perhaps maximizes van der Waals contacts and contributes to favorable binding enthalpy. Additionally, the fused benzoxazole-like pattern favorably orients dipoles for potential water-mediated contacts without introducing the excessive polarity observed in aldehyde-containing analogues. The compound designated as **13** is a little less effective than compound **11,** probably due to the presence of a para-aldehyde substituent on the aromatic ring, with a polar, reactive carbonyl group. This particular functional group may influence the hydrophobicity necessary for optimal accommodation within the inhibitory pocket, potentially resulting in a marginal reduction in activity. Furthermore, the electron-withdrawing properties of the aldehyde diminish electron density throughout the aromatic system, thereby impairing the benzyloxy oxygen's capacity to engage in stabilizing interactions. Compound **12** bears the same para-aldehyde substituent on the aromatic ring but also contains a meta-methoxy group, which may affect its inhibitory activity compared to **11** and **13**. Ultimately, compound **14** contains a para-aldehyde and two moderately bulky ortho-methoxy groups, which may increase the steric hindrance of the ligand due to their protruding methyl units, and may physically prevent the regular interactions within the ATP-binding pocket.

Despite its potent inhibition of the PKA Cα-subunit in a cell-free enzymatic assay, compound **11** shows no cytotoxicity, underscoring the distinction between biochemical target inhibition and cellular efficacy. Although enzyme-based assays provide direct evidence of target interaction, they do not account for factors such as solubility, membrane permeability, intracellular distribution, or efflux mechanisms, all of which strongly influence cellular responses [40]. Compound **11** binds efficiently to the ATP-binding pocket of PKA, as supported by docking and low-micromolar $IC_{50}$ values. However, its pronounced lipophilicity, conferred by the para-allyl substituent, may limit effective intracellular target interaction. Highly lipophilic compounds are known to have reduced aqueous solubility and to preferentially partition into lipid membranes. This can significantly lower the free cytosolic concentration required for effective kinase inhibition in cells [41]. Furthermore, the selective inhibition of the PKA Cα-subunit alone may be insufficient to induce antiproliferative effects in the tested cancer cell lines. PKA regulates diverse, context-dependent signaling pathways and functions as either a pro-survival or pro-apoptotic mediator, depending on the cellular background and signaling state [42]. In many tumor models, partial inhibition of a single kinase can be compensated for by parallel or redundant signaling pathways, resulting in limited effects on cell viability [43]. In contrast, compounds in this series that exhibited cytotoxic activity may affect multiple kinases or signaling nodes. This is consistent with the idea that polypharmacology correlates with anticancer efficacy [44]. Taken together, these observations suggest that compound **11** is a potent, selective biochemical inhibitor of PKA. However, it lacks the physicochemical and signaling network disruption necessary to translate enzymatic inhibition into measurable cytotoxicity.

One of the most studied regions of the catalytic subunit of PKA is the G-loop, located at the protein's active site. As a highly conserved structural element, the G-loop provides crucial flexibility to accommodate the ATP molecule and orient it for catalysis. This loop undergoes conformational changes during the phosphorylation reaction, facilitating the transfer of the γ-phosphate from ATP to the substrate [45]. Since ATP protected against inhibition and all four compounds (**11**–**14**) share a scaffold structure consisting of a quinoline–triazole core, they may be classified as Type I protein kinase inhibitors. In general, Type I inhibitors contain a heterocyclic moiety that occupies the purine-binding pocket and acts as an ATP-binding site competitor, mimicking the purine ring of ATP [46]. For example, the ATP binding site is highly conserved across the kinome [47], which may lead to off-target effects. Then, the application of PKA inhibitors presents clear challenges. For this reason, developing novel inhibitors should focus on exploiting unique PKA conformations, allosteric sites, or substrate-binding domains to achieve greater selectivity and overall efficacy.

Evidence from cell lines suggests that these compounds might also impact other protein kinases different than PKA, though causal proof is missing, and attributing these effects to other kinases remains speculative. For instance, compounds **14** and **20** showed selectivity for T-cell leukemia, implying potential involvement of tyrosine kinases related to T-cell activation. In platelets, interactions between PKC, PKA, and PP2A, and both BTK and Syk, have been studied [48]. The results suggest that these three enzymes (PKC, PKA, and PP2A) can modulate BTK and Syk, which are critical kinases in B-cell leukemia and may explain the effects of compound **13**. Compound **19** was specific to A549 cells and showed moderate specificity for B-cell lines, indicating potential effects on Src kinases. Recently, it has also been demonstrated that A549 proliferation is affected by PI3K/AKT/mTOR, MAPK, and Wnt signaling pathways, which differ in part from the principal signal transduction pathways used in the other cell lines studied [49]. Compound **19** might affect PI3K and Wnt signaling cascades, which are crucial



18607187, 2026, 15, Downloaded from https://chemistry-europe.onlinelibrary.wiley.com/doi/10.1002/cmdc.70425 by University Palacky, Wiley Online Library on [06/08/2026]. See the Terms and Conditions (https://onlinelibrary.wiley.com/terms-and-conditions) on Wiley Online Library for rules of use; OA articles are governed by the applicable Creative Commons License

for the survival of several tumor cell lines [50]. Compound **12** was selective for the p53 KO cell line, likely influencing p53-dependent cell cycle regulation, whereas compound **22** affected all tumor cell lines except A549, which suggests an effect on different signaling routes. Other structures appeared to be involved in broader, nonspecific signaling pathways.

It is important to remember that results from cell-based assays often indicate multikinase effects or polypharmacological activity. The biological activity of the compounds used here was moderate, with $IC_{50}$ values in the micromolar range. Micromolar potency often correlates with widespread off-target effects across the kinome and a more extensive kinome profiling panel is necessary to precisely identify secondary targets. Having experimentally demonstrated PKA inhibition for selected compounds, it is conceivable that these structural scaffolds might also modulate parallel signaling networks like BTK, Src, or PI3K/AKT. However, because direct biochemical evidence for these multikinase interactions is currently lacking, these downstream effects are presented strictly as mechanistically plausible hypotheses that warrant future experimental validation. In conclusion, we have identified a novel series of preliminary small-molecule leads. Although their current biological activity resides primarily in the micromolar $IC_{50}$ range, the moderate selectivity observed provides a valuable baseline for structural optimization in future anticancer drug discovery campaigns.

## 3 | Conclusion

Hybrid compounds containing a quinoline unit coupled to natural phenols represent a new class of therapeutically interesting compounds. For the synthesis, we used a 1,2,3-triazole species as a coupling connector, prepared via a well-known Cu(I)-catalyzed azide–alkyne cycloaddition reaction. The various synthesized compounds elicited a diversity of responses, with only structures **11**, **15**, and **16** showing no cytotoxicity effect on any cell line, and compound **17** affecting both normal and cancer cells. Compound **13** was the most promising due to its cytotoxicity against most of the tumor cell lines except A549. In addition, compound **13** markedly affected B-cell leukemia cell lines, although no effect on primary lymphocytes or normal cell lines was observed. Compounds **14** and **20** were highly specific for T-cell leukemia, whereas compound **19** was specific for A549 and moderately specific for B-cell lines. Compound **12** specifically affected the human colorectal carcinoma HCTp53 KO and T-cell leukemia CCRF-CEM cell lines. Compound **22** displayed unique effects by inducing cell death in leukemic and colon carcinoma lines but not lung cancer lines. In vitro assays and computational molecular docking identified compounds **11**–**14** as binders to the PKA Cα-subunit, suggesting a protein kinase-targeted anticancer mechanism. Although compound **11** was the most effective PKA inactivator agent, its lack of cytotoxicity highlights the importance of physicochemical properties and intracellular target accessibility in determining cellular efficacy. Docking studies also indicated that the quinoline–triazole scaffold was capable of occupying the ATP-binding pocket of the PKA Cα-subunit, since the compounds established interactions with key residues that are involved in nucleotide recognition and/or are located in the active site of the enzyme. Overall, this study provides valuable structure–activity insights that may guide the rational optimization of quinoline–triazole hybrid derivatives toward improved cellular potency and therapeutic potential.

## 4 | Experimental Section

### 4.1 | Chemistry

Fourier transform infrared (FTIR) spectroscopy was performed using a Perkin-Elmer Spectrum Two instrument equipped with a Diamond/ZnSe attenuated total reflectance (ATR) sampling accessory (Waltham, MA, USA). Measurements were taken at room temperature, with 64 scans per minute per analysis, a resolution of 0.5 $cm^{-1}$, and a spectral range of 4000–450 $cm^{-1}$. $^1H$ and $^{13}C$ NMR spectra were recorded on a Nanalysis 100 MHz PRO Benchtop spectrometer (Calgary, AB, Canada) operating at 100 MHz for $^1H$ and 25.8 MHz for $^{13}C$. $CDCl_3$ or dimethyl sulfoxide (DMSO-$d_6$) was used as a solvent. Chemical shifts are reported in ppm downfield from the residual solvent peaks: $\delta$ 7.25 for $^1H$ NMR and 77.0 for $^{13}C$ NMR in $CDCl_3$, and δ 2.54 for $^1H$ NMR and 44.5 for $^{13}C$ NMR in DMSO-$d_6$. Mass spectra were obtained using an Agilent GC–MS model 5977C spectrometer with electron ionization (EI) at 70 eV, coupled directly to an Agilent model 8860 gas chromatograph (Wilmington, DE, USA). Elemental analyses were conducted with a Perkin-Elmer 2400 CHN elemental analyzer, yielding results within ±0.4% of the theoretical values. Melting points were determined using a Fisher–Johns fusiometer (Thermo Fisher Scientific, Waltham, MA, USA) and are reported uncorrected. Thin-layer chromatography (TLC) was performed on Merck silica F254 plates (0.25 mm thickness; Darmstadt, Germany), with spots visualized under UV light at 254 nm. All chemical reagents were purchased from Aldrich Chemical Co. (St. Louis, MO, USA). All solvents were distilled and dried by standard procedures before use.

### 4.2 | General Procedure for the Synthesis of Methoxy-4-(prop-2-yn-1-yloxy)derivatives 3–8

To a solution of compounds **1a**–**f** (5.0 mmol) in dry acetone, $K_2CO_3$ (15 mmol) was added, and the mixture was stirred at room temperature (rt) for 5 min. Propargyl bromide (5.0 mmol) was added, and the resulting mixture was heated to 60–65 °C for 12 h, at which point TLC indicated the reaction was complete. The reaction mixture was diluted with 50 mL of water and extracted with ethyl acetate (3 × 50 mL). The organic extracts were combined, washed with a 7.5% KOH solution (2 × 20 mL) and brine (2 × 10 mL), dried over anhydrous $Na_2SO_4$, and concentrated under a rotavapor to obtain pure compounds **3**–**8** in good yields.

#### *4.2.1 | 4-Allyl-2-Methoxy-1-(Prop-2-yn-1-yloxy)benzene 3 [51]*

Yellow solid, Yield: 92%, FTIR (ATR) $cm^{-1}$: 3288, 2936, 1638, 1592, 1508, 1259, 1216, 1139, 996, 803; $^1H$ NMR (100 MHz, $CDCl_3$) δ: 2.54 (t, 1H, $J = 2$ Hz), 3.37 (d, 2H, $J = 6$ Hz), 3.92 (s, 3H, $OCH_3$), 4.78 (d, 2H, $J = 2$ Hz), 5.07–5.21 (m, 2H,



18607187, 2026, 15, Downloaded from https://chemistry-europe.onlinelibrary.wiley.com/doi/10.1002/cmdc.70425 by University Palacky, Wiley Online Library on [06/08/2026]. See the Terms and Conditions (https://onlinelibrary.wiley.com/terms-and-conditions) on Wiley Online Library for rules of use; OA articles are governed by the applicable Creative Commons License

=$CH_2$), 6.23–5.84 (m, 1H, =CH), 6.71–6.85 (m, 2H, Ar), 7.04 (d, 1H, $J = 8$ Hz); $^{13}$C NMR (25.8 MHz, $CDCl_3$) δ: 39.9, 55.9, 57.2, 75.5, 78.4, 112.7, 115.3, 115.7, 120.5, 134.5, 137.5, 145.4, 149.9. MS, m/z (%) 202.10 [M] (40), 163.08 [M-$C_3H_3$] (100), 161.06 [M-$C_3H_4$] (5), 131.04 [$C_9H_6O$] (12), 105.07 [$C_7H_5O$] (16), 91.03 [M-$C_6H_3O$] (45).

#### 4.2.2 | 3-Methoxy-4-(Prop-2-yn-1-yloxy)benzaldehyde 4

White solid, Yield: 87%, Mp: 86 °C, Lit. (86 °C) [52, 53], FTIR (ATR) cm$^{-1}$: 3247, 3021, 1688, 1587, 1506, 1261, 1134, 1001, 804; $^1$H NMR (100 MHz, $CDCl_3$) δ: 2.61 (t, 1H, $J = 2$ Hz), 3.99 (s, 3H, $OCH_3$), 4.90 (d, 2H, $J = 2$ Hz), 7.17 (d, 1H, $J = 8$ Hz), 7.47–7.56 (m, 2H, Ar), 9.92 (s, 1H, CHO); $^{13}$C NMR (25.8 MHz, $CDCl_3$) δ: 56.1, 56.7, 76.6, 77.4, 109.8, 112.9, 126.1, 131.2, 150.2, 152.3, 190.8; MS, m/z 190.06 [M] (69), 161.04 [M-CHO] (11), 151.04 [M-$C_3H_3$] (100), 105.03 [$C_7H_5O$] (9), 91.03 [$C_6H_3O$] (9).

#### 4.2.3 | 1-(4-Methoxy-2-(Prop-2-yn-1-yloxy)phenyl)ethan-1-one 5

White solid, Yield: 97%, Mp: 75–76 °C, Lit. (74.7 °C) [15], FTIR (ATR) cm$^{-1}$: 3275, 2999, 1647, 1599, 1430, 1253, 1015, 965, 827; $^1$H NMR (100 MHz, $CDCl_3$) δ: 2.61 (t, 1H, $J = 2$ Hz), 2.66 (s, 3H, $CH_3$), 3.90 (s, 3H, $OCH_3$), 4.55 (d, 2H, $J = 2$ Hz), 6.58–6.69 (m, 2H, Ar), 7.88 (d, 1H, $J = 9$ Hz); $^{13}$C NMR (25.8 MHz, $CDCl_3$) δ: 27.6, 55.6, 56.3, 76.3, 77.1, 99.9, 106.3, 121.9, 132.7, 164.3, 189.4, 205.6; (EI) m/z (%): 204.08 [M] (16), 189.05 [M-$CH_3$] (51), 161.06 [M-$C_2H_3O$] (100), 136.04 [$C_8H_8O_2$] (4).

#### 4.2.4 | 1-Isopropyl-4-Methyl-2-(Prop-2-yn-1-yloxy)benzene 6 [54]

Yellow solid, Yield: 93%, FTIR (ATR) cm$^{-1}$: 3292, 2960, 2869, 1612, 1578, 1504, 1244, 1162, 1036, 810; $^1$H NMR (100 MHz, $CDCl_3$) δ: 1.29 (d, 6H, $J = 7$ Hz), 2.42 (s, 3H, $CH_3$), 2.56 (t, 1H, $J = 2$ Hz), 3.40 (q, 1H, $J = 7$ Hz), 4.78 (d, 2H, $J = 2$ Hz), 6.85–6.92 (m, 2H, Ar), 7.20 (d, 1H, $J = 8$ Hz); $^{13}$C NMR (25.8 MHz, $CDCl_3$) δ: 21.3, 22.9, 26.6, 56.2, 75.0, 79.3, 113.3, 122.3, 126.2, 134.9, 136.3, 154.9; (EI) m/z (%): 188.13 [M] (41), 173.10 [M-$CH_3$] (38), 158.00 [M-$C_2H_6$] (24), 145.09 [M-$C_3H_7$] (100), 133.08 [M-$C_3H_3O$] (12); Anal. Calcd for $C_{13}H_{16}O$: C, 82.94; H, 8.57. Found: C, 82.95; H, 8.63.

#### 4.2.5 | 3,5-Dimethoxy-4-(Prop-2-yn-1-yloxy)benzaldehyde 7

Beige solid, Yield: 87%, Mp: 101–102 °C, FTIR (ATR) cm$^{-1}$: 3277, 2965, 1687, 1590, 1456, 1327, 1231, 1122, 995, 835; $^1$H NMR (100 MHz, $CDCl_3$) δ: 2.49 (t, 1H, $J = 2$ Hz), 3.98 (s, 6H, 2 × $OCH_3$), 4.88 (d, 2H, $J = 2$ Hz), 7.18 (s, 2H, Ar), 9.92 (s, 1H, CHO); $^{13}$C NMR (25.8 MHz, $CDCl_3$) δ: 56.4, 60.0, 75.4, 106.7, 126.7, 132.4, 143.3, 154.1, 190.8; MS, m/z 220.05 [M] (24), 181.05 [M-$C_3H_3$] (100), 152.06 [$C_8H_8O_3$] (2), 136.02 [$C_8H_8O_2$] (8), 120.99 [$C_7H_5O_2$] (5), 103.07 [$C_7H_3O$] (1); Anal. Calcd for $C_{12}H_{12}O_4$: C, 65.45; H, 5.49. Found: C, 65.47; H, 5.53.

#### 4.2.6 | 4-(Prop-2-yn-1-yloxy)benzaldehyde 8

White solid, Yield: 93%, Mp: 76–77 °C (77–79 °C) [55], FTIR (ATR) cm$^{-1}$: 3229, 2953, 1670, 1586, 1508, 1436, 1261, 1130, 1013, 810; $^1$H NMR (100 MHz, $CDCl_3$) δ: 2.62 (t, 1H, $J = 2$ Hz), 4.82 (d, 2H, $J = 2$ Hz), 7.23 (d, 2H, $J = 8$ Hz), 7.86 (d, 2H, $J = 8$ Hz), 9.94 (s, 1H, CHO); $^{13}$C NMR (25.8 MHz, $CDCl_3$) δ: 56.0, 76.4, 115.3, 126.9, 130.7, 131.9, 162.4, 190.7; Anal. Calcd for $C_{10}H_8O_2$: C, 74.99; H, 5.03. Found: C, 74.93; H, 5.07.

### 4.3 | General Procedure for Synthesis of 4-Azido-7-Chloroquina 9,10

The required intermediates **9** and **10** were prepared using a partially modified procedure previously reported by de Souza et al. [56]. All compounds were characterized using spectral data. In general, the $^1$H NMR spectrum displayed the five quinoline protons in the range of 6.66–8.91 ppm and the aliphatic protons at 3.69–3.75 ppm. The $^{13}$C NMR spectrum showed the nine quinoline carbon signals in the region of 99.0–150.7 ppm, while the aliphatic carbon signals appeared at 42.3–49.9 ppm. Additionally, the IR spectra of both compounds showed characteristic absorption peaks for the $N_3$ (azide) group near 2124 cm$^{-1}$, confirming the formation of intermediates **9** and **10** [49].

#### 4.3.1 | 4-Azido-7-Chloroquinoline 9

White solid, Yield: 91%, mp: 110–112 °C (110–112 °C) [56].

#### 4.3.2 | N-(2-Azidoethyl)-7-Chloroquinolin-4-Amine 10

White solid, Yield: 84%, mp: 137–139 °C (145–147 °C) [56].

### 4.4 | General Procedure for the Preparation of Compounds 7-Chloro-4-(1H-1,2,3-triazol-1-yl) quinolines 11–16 and N-(4-(1H-1,2,3-triazol-1-yl) ethyl)-7-Chloroquinolin-4-Amine 17–22

A mixture of *tert*-BuOH/$H_2O$ (1:1) (8 mL) was added to 4-Azido-7-chloroquinoline **9** or *N*-(2-Azidoethyl)-7-chloroquinolin-4-amine **10** (1.1 mmol), the appropriate acetylene (1.0 mmol), L-ascorbic acid sodium salt (0.28 mmol), and $CuSO_4{\cdot}5H_2O$ (0.07 mmol). The reaction mixture was stirred vigorously at rt for 12 h. The progress of TLC was used to monitor the reaction (DCM/methanol 9.5:0.5). Upon completion, the reaction mixture was poured into ice-cold water (15 mL) and extracted with ethyl acetate (2 × 20 mL). The organic extracts were then combined, washed with water (2 × 10 mL) and brine (2 × 10 mL), dried over anhydrous $Na_2SO_4$, and concentrated using a rotavapor. The residual crude product was purified by silica gel column chromatography using a mixture of DCM/MeOH (9.5/0.5) as the eluent to obtain compounds **11–22**.

#### 4.4.1 | 4-(4-((4-Allyl-2-methoxyphenoxy)methyl)-1H-1,2,3-triazol-1-yl)-7-Chloroquinoline 11

White solid, Yield: 91%, Mp: 114 °C, IR cm$^{-1}$: 3149, 1610, 1591, 1560, 1512, 1257, 1223, 1135, 992, 804; $^1$H NMR (100 MHz, $CDCl_3$), δ: 3.41 (d, 2H, $CH=CH_2$, $J = 6.5$ Hz), 3.93 (s, 3H, $OCH_3$), 5.07 (m, 2H, $CH_2$), 5.48 (s, 2H, $CH_2$), 5.83–6.16 (m, 1H, =CH=), 6.77–6.83 (m, 2H, H3′, 5′), 7.08 (d, 1H, H6′, $J = 9$ Hz), 7.54 (d, 1H, H3, $J = 5$ Hz), 7.64 (dd, 1H, H6, $J_1 = 9$ Hz, $J_2 = 2$ Hz), 8.02 (d, 1H, H5, $J = 9$ Hz), 8.16 (s, 1H,



18607187, 2026, 15, Downloaded from https://chemistry-europe.onlinelibrary.wiley.com/doi/10.1002/cmdc.70425 by University Palacky, Wiley Online Library on [06/08/2026]. See the Terms and Conditions (https://onlinelibrary.wiley.com/terms-and-conditions) on Wiley Online Library for rules of use; OA articles are governed by the applicable Creative Commons License

H5″), 8.3 (d, 1H, H8, $J = 2$ Hz), 9.11 (d, 1H, H2, $J = 5$ Hz); $^{13}$C NMR (25.8 MHz, $CDCl_3$), δ: 33.8, 55.9, 63.6, 112.4, 112.7, 115.3, 115.8, 116.1, 120.7, 124.7, 129.0, 129.4, 134.5, 136.9, 137.4, 140.9, 145.5, 149.9, 150.2, 151.4; (EI) m/z (%): 378.13 [M+-$C_2H_3$] (100), 162.00 [M+- $C_{13}H_{14}N_3O_2$] (63), 177.09 [M+-$C_{11}H_{13}O_2$] (31), 147.06 [M+- $C_{10}H_{11}O$] (32), 102.04 [$C_7H_4N$] (21); Anal. Calcd for $C_{22}H_{19}ClN_4O_2$: C, 64.95; H, 4.71; N, 13.77. Found: C, 65.02; H, 4.70; N, 14.09.

#### *4.4.2 | 4-((1-(7-Chloroquinolin-4-yl)-1H-1,2,3-triazol-4-yl) methoxy)-3-Methoxybenzaldehyde 12*

Beige solid, Yield: 83%, Mp: 80–82 °C, Lit. (137–138 °C) [52], IR cm$^{-1}$: 3082, 1684, 1589, 1509, 1455, 1264, 1135, 987, 805; $^1$H NMR (100 MHz, $CDCl_3$), δ: 4.00 (s, 3H, $OCH_3$), 5.59 (s, 2H, $CH_2$), 7.28–7.70 (m, 4H, Ar), 8.01 (d, 1H, H5, $J = 9$ Hz), 8.21 (s, 1H, H5″), 9.11 (d, 1H, H2, $J = 5$ Hz), 9.94 (s, 1H, CHO); $^{13}$C NMR (25.8 MHz, $CDCl_3$), δ: 56.1, 62.9, 109.8, 112.9, 116.1, 123.8, 124.5, 125.0, 126.4, 127.3, 129.0, 129.4, 131.1, 136.9, 140.8, 144.3, 150.2, 151.3, 190.7; (EI) m/z (%): 366.11 [M-CHO] (45), 207.05 [$C_{12}H_8N_4$] (100), 162.05 [$C_9H_5ClN$] (29), 102.09 [$C_7H_4N$] (26); Anal. Calcd for $C_{20}H_{15}ClN_4O_3$: C, 60.84; H, 3.83; N, 14.19. Found: C, 60.91; H, 3.86; N, 14.41.

#### *4.4.3 | 4-((1-(7-Chloroquinolin-4-yl)-1H-1,2,3-triazol-4-yl) methoxy)benzaldehyde 13*

Beige solid, Yield: 81%, Mp: 184 °C, IR cm$^{-1}$: 3065, 1688, 1594, 1510, 1434, 1264, 1164, 1006, 844; $^1$H NMR (100 MHz, $CDCl_3$), δ: 5.52 (s, 2H, $CH_2$), 7.22 (d, 2H, H2′, 6′, $J = 8$ Hz), 7.56 (d, 1H, H3, $J = 5$ Hz), 7.65 (dd, 1H, H6, $J_1 = 8$ Hz, $J_2 = 2$ Hz), 7.90–8.07 (m, 3H, Ar), 8.19 (s, 1H, 5H″), 8.32 (d, 1H, H8, $J = 2$ Hz), 9.12 (d, 1H, H2, $J = 5$ Hz), 9.98 (s, 1H, CHO); $^{13}$C NMR (25.8 MHz, $CDCl_3$), δ: 61.8, 115.8, 117.6, 125.8, 128.7, 129.5, 130.4, 132.3, 136.1, 143.6, 148.6, 152.8, 163.5, 168.3, 170.8, 191.8; (EI) m/z (%): 336.04 [M-CHO] (20), 207.07 [$C_{12}H_8N_4$] (100), 162.03 [$C_9H_5ClN$] (17), 101.90 [$C_7H_4N$] (10); Anal. Calcd for $C_{19}H_{13}ClN_4O_2$: C, 62.56; H, 3.59; N, 15.36. Found: C, 62.58; H, 3.64; N, 15.57.

#### *4.4.4 | 4-((1-(7-Chloroquinolin-4-yl)-1H-1,2,3-triazol-4-yl) methoxy)–3,5-Dimethoxybenzaldehyde 14*

White solid, Yield: 76%, Mp: 167–168 °C, IR cm$^{-1}$: 2952, 1692, 1592, 1501, 1451, 1328, 1228, 1125, 994, 877; $^1$H NMR (100 MHz, $CDCl_3$), δ: 4.00 (S, 6H, 2 x $OCH_3$), 5.53 (s, 2H, $CH_2$), 7.22 (s, 2H, H2′, 6′), 7.54–7.59 (m, 2H, H3, 6), 7.99 (d, 1H, H5, $J = 8$ Hz), 8.24 (s, 1H, 5H″), 8.32 (d, 1H, H8, $J = 2$ Hz), 9.12 (d, 1H, H2, $J = 5$ Hz), 9.95 (s, 1H, CHO); $^{13}$C NMR (25.8 MHz, $CDCl_3$), δ: 56.4, 66.3, 106.8, 116.1, 124.5, 124.9, 129.1, 129.4, 132.5, 136.9, 141.0, 141.7, 145.8, 150.2, 151.4, 153.9, 190.8; (EI) m/z (%): 396.14 [M+- CHO] (10), 230.07 [M-$C_{10}H_{11}O_4$] (33), 207.03 [$C_{12}H_8N_4$] (100), 166.08 [M-$C_{12}H_8ClN_4O$] (33), 97.05 [ $C_3H_3N_3O$] (11); Anal. Calcd for $C_{21}H_{17}ClN_4O_4$: C, 59.37; H, 4.03; N, 13.19. Found: C, 59.39; H, 4.07; N, 12.95.

#### *4.4.5 | 7-Chloro-4-(4-((2-Isopropyl-5-methylphenoxy)methyl)-1H-1,2,3-triazol-1-yl)quinoline 15*

Yellow solid, Yield: 87%, IR cm$^{-1}$: 2959, 2923, 2868, 1611, 1561, 1504, 1252, 1027, 878, 811; $^1$H NMR (100 MHz, $CDCl_3$), δ: 1.26 (d, 6H, $CH_3$, $J = 7$ Hz), 2.41 (s, 3H, $CH_3$), 3.38 (sex, 1H, CH, $J = 7$ Hz), 5.45 (s, 2H, $CH_2$), 6.85–6.92 (m, 2H, H4′, 6′), 6.18 (d, 1H, H3′, $J = 8$ Hz), 7.57 (d, 1H, H3, $J = 5$ Hz), 7.65 (dd, 1H, H6, $J_1 = 9$ Hz, $J_2 = 2$ Hz), 8.03 (d, 1H, H5, $J = 9$ Hz), 8.11 (s, 1H, 5H″), 8.31 (d, 1H, H8, $J = 2$ Hz), 9.11 (d, 1H, H2, $J = 5$ Hz); $^{13}$C NMR (25.8 MHz, $CDCl_3$), δ: 21.3, 22.9, 26.7, 62.5, 113.1, 116.2, 120.7, 122.3, 124.1, 124.6, 126.3, 129.1, 136.6, 137.1, 141.0, 145.1, 150.2, 151.4, 155.3, 161.9, 169.9; (EI) m/z (%): 392.14 [M] (2), 364.10 [$C_{20}H_{17}ClN_4O$] (59), 349.07 [M-$C_3H_7$] (29), 215.03 [$C_{12}H_{14}N_3O$] (16), 162.02 [M-$C_{13}H1_6N_3O$] (31), 135.06 [M-$C_{12}H_8ClN_4O$] (100), 97.07 [$C_3H_3N_3O$] (4), 81.06 [$C_3H_3N_3$] (22); Anal. Calcd for $C_{22}H_{21}ClN_4O$: C, 67.26; H, 5.39; N, 14.26 Found: C, 67.35; H, 5.42; N, 14.53.

#### *4.4.6 | 1-(2-((1-(7-Chloroquinolin-4-yl)-1H-1,2,3-triazol-4-yl) methoxy)-4-Methoxyphenyl)ethan-1-one 16*

White solid, Yield: 89%, Mp: 143–144 °C, IR cm$^{-1}$: 3052, 2982, 1645, 1600, 1501, 1439, 1328, 1261, 1124, 966, 812; $^1$H NMR (100 MHz, $CDCl_3$), δ: 2.62 (s, 3H, $CH_3$), 3.91 (s, 3H, $OCH_3$), 5.47 (s, 2H, $CH_2$), 6.61 (dd, 1H, H5′, $J_1 = 8$ Hz, $J_2 = 3$ Hz), 6.73 (d, 1H, H3′, $J = 3$ Hz), 7.54 (d, 1H, H3, $J = 5$ Hz), 7.62 (dd, 1H, H6, $J_1 = 9$ Hz, $J_2 = 2$ Hz), 7.84 (d, 1H, H6′, $J_1 = 8$ Hz), 7.96 (d, 1H, H5, $J = 8$ Hz), 8.22 (s, 1H, 5H″), 8.27 (d, 1H, H8, $J = 2$ Hz), 9.09 (d, 1H, H2, $J = 2$ Hz); $^{13}$C NMR (25.8 MHz, $CDCl_3$), δ: 31.6, 55.7, 62.6, 100.0, 106.2, 116.1, 121.7, 124.4, 124.8, 129.1, 129.6, 132.9, 137.0, 144.4, 150.3, 151.4, 159.3, 164.5, 197.5; (EI) m/z (%): 405.02 [M] (4), 379.04 [M-$CH_3O$] (3), 364.86 [M-$C_2H_3O$] (2), 206.98 [$C_{12}H_8N_4$] (100), 192.98 [$C_{11}H_6N_4$] (13), 165.00 [M-$C_{12}H_8ClN_4$] (7), 135.02 [$C_8H_6O_2$] (17), 96.05 [$C_3H_3N_3O$] (29), 81.02 [$C_3H_3N_3$] (45); Anal. Calcd for $C_{21}H_{17}ClN_4O_3$: C, 61.69; H, 4.19; N, 13.70. Found: C, 61.71; H, 4.23; N, 13.92.

#### *4.4.7 | N-(2-(4-((4-Allyl-2-methoxyphenoxy)methyl)-1H-1,2,3-triazol-1-yl)ethyl)-7-Chloroquinolin-4-Amine 17*

Beige solid, Yield: 86%, Mp: 150–152 °C, IR cm$^{-1}$: 3351, 3251, 3218, 2937, 1610, 1587, 1515, 1260, 1223, 1140, 997, 805, 793; $^1$H NMR (100 MHz, $CDCl_3$) δ: 3.35 (d, 2H, $CH = CH_2$, $J = 6.5$ Hz), 3.83 (s, 3H, $OCH_3$), 3.97 (t, 2H, 2H, H9, $J = 5.7$ Hz), 4.74 (t, 2H, H10, $J = 5.7$ Hz), 5.10 (m, 2H, $CH_2$), 5.25 (s, 2H, $CH_2$), 5.96 (m, 1H, =CH═), 6.44 (d, 1H, H3, $J = 4$ Hz), 6.74 (m, 2H, H3′, 5′), 6.94 (d, 1H, H6′, $J = 8$ Hz), 7.35 (m, 1H, Ar), 7.84 (m, 3H, Ar), 8.51 (brs, 1H, $H_2$); $^{13}$C NMR (25.8 MHz DMSO $d_6$), δ: 39.8, 42.7, 48.6, 55.8, 63.3, 112.6, 114.6, 115.8, 120.6, 123.0, 125.9, 133.3, 134.5, 135.4, 137.4, 145.7, 149.6, 152.3; (EI) m/z (%): 207.04 [M-$C_{13}H_{14}N_3O_2$] (100), 162.94 [$C_{10}H_{11}O_2$] (2), 97.05 [$C_3H_3N_3O$] (3); Anal. Calcd for $C_{24}H_{24}ClN_5O_2$: C, 64.07; H, 5.38; N, 15.57. Found: C, 63.98; H, 5.43; N, 15.79.

#### *4.4.8 | 4-((1-(2-((7-Chloroquinolin-4-yl)amino)ethyl)-1H-1,2,3-triazol-4-yl)methoxy)-3-Methoxybenzaldehyde 18*

Beige solid, Yield: 82%, Mp: 210 °C, IR cm$^{-1}$: 3324, 3170, 1674, 1585, 1265, 1221, 983, 805; $^1$H NMR (100 MHz, $CDCl_3$) δ: 3.83 (m, 5H, $CH_2$, $OCH_3$), 4.74 (t, 2H, H10, $J = 6$ Hz), 4.96 (brs, 1H, NH), 5.28 (s, 2H, $CH_2$), 6.59 (brs, 1H, H3), 7.21–7.59 (m, 4H, Ar), 7.55 (brs, 1H, Ar), 8.14–8.23 (m, 2H, Ar, 5H″), 9.87 (s, 1H, CHO); $^{13}$C NMR (25.8 MHz DMSO $d_6$), δ: 42.9, 48.5,



18607187, 2026, 15, Downloaded from https://chemistry-europe.onlinelibrary.wiley.com/doi/10.1002/cmdc.70425 by University Palacky, Wiley Online Library on [06/08/2026]. See the Terms and Conditions (https://onlinelibrary.wiley.com/terms-and-conditions) on Wiley Online Library for rules of use; OA articles are governed by the applicable Creative Commons License

55.5, 62.3, 110.5, 113.2, 124.2, 124.9, 125.2, 126.2, 130.5, 142.5, 143.7, 149.8, 153.3, 191.8; (EI) m/z (%): 438.03 [M+] (1.8), 409.05 [M-CHO] (6), 286.00 [M-$C_8H_7O_3$] (5), 207.03 [M-$C_{11}H_{10}N_3O_3$] (100), 163.02 [$C_{10}H_{11}O_2$] (5), 96.05 [$C_3H_3N_3O$] (13); Anal. Calcd for $C_{22}H_{20}ClN_5O_3$: C, 60.35; H, 4.60; N, 15.99. Found: C, 60.39; H, 4.62; N, 16.23.

#### *4.4.9 | 4-((1-(2-((7-Chloroquinolin-4-yl)amino)ethyl)-1H-1,2,3-triazol-4-yl)methoxy)-Benzaldehyde 19*

White solid, Yield: 89%, Mp: 176–178 °C, IR $cm^{-1}$: 3316, 3113, 1672, 1582, 1509, 1255, 1157, 998, 866; $^1H$ NMR (100 MHz, DMSO $d_6$), δ: 2.86 (d, $CH_2$, H9, $J = 6$ Hz), 4.72 (t, 2H, H10, $J = 6$ Hz), 5.28 (s, 2H, $CH_2$), 6.55 (d, 1H, H3, $J = 5$ Hz), 7.24 (d, 2H, H2′, 6′, $J = 8$ Hz), 7.43–7.52 (m, 2H, Ar, NH), 7.83–7.92 (m, 3H, Ar), 8.16 (d, 1H, H5, $J = 8$ Hz), 8.29 (s, 1H, 5H″), 8.42 (brs, 1H, H2), 9.90 (s, 1H, CHO); $^{13}C$ NMR (25.8 MHz, DMSO $d_6$), δ: 42.1, 48.5, 62.0, 115.7, 124.4, 124.8, 125.7, 128.1, 130.4, 132.2, 134.1, 142.5, 150.2, 156.1, 163.5, 191.8; (EI) m/z (%): 407.05 [M] (1), 379.15 [M-CHO] (11), 207.05 [M-$C_{10}H_8N_3O_2$] (100), 162.95 [$C_{10}H_{11}O_2$] (5), 96.02 [$C_3H_3N_3O$] (13); Anal. Calcd for $C_{21}H_{18}ClN_5O_2$: C, 61.84; H, 4.45; N, 17.17. Found: C, 61.92; H, 4.51; N, 17.55.

#### *4.4.10 | 4-((1-(2-((7-Chloroquinolin-4-yl)amino)ethyl)-1H-1,2,3-triazol-4-yl)methoxy)−3,5-Dimethoxybenzaldehyde 20*

Yellow solid, Yield: 76%, Mp: 158–160 °C, IR $cm^{-1}$: 3192, 3123, 1689, 1577, 1497, 1326, 1120, 987, 853; $^1H$ NMR (100 MHz, DMSO $d_6$), δ: 3.74–3.87 (m, 8H, $CH_2$, 2 x $OCH_3$), 4.70 (t, 2H, H10, $J = 6$ Hz), 5.10 (s, 2H, $CH_2$), 6.54 (d, 1H, H3, $J = 5$ Hz), 7.23 (s, 2H, H2′, 6′), 7.47 (dd, 1H, H6, $J_1 = 8$, $J_2 = 2$ Hz), 7.83 (d, 1H, H8, $J = 2$ Hz), 8.17–8.22 (m, 2H, H5″, H5), 8.29 (s, 1H, 5H″), 8.44 (brs, 1H, H2), 9.88 (s, 1H, CHO); $^{13}C$ NMR (25.8 MHz, DMSO $d_6$), δ: 42.9, 48.2, 56,6, 65.9, 107.3, 124.2, 124.8, 125.0, 125.4, 128.8, 132.4, 150.3, 154.0, 173.1, 192.3; (EI) m/z (%): 467.08 [M+] (1.2), 438.05 [M-CHO] (5), 207.05 [M-$C_{12}H_{12}N_3O_4$] (100)162.95 [$C_{10}H_{11}O_2$] (5), 96.02 [$C_3H_3N_3O$] (6); Anal. Calcd for $C_{23}H_{22}ClN_5O_4$: C, 59.04; H, 4.74; N, 14.97. Found: C, 58.97; H, 4.73; N, 15.19.

#### *4.4.11 | 7-Chloro-N-(2-(4-((2-Isopropyl-5-methylphenoxy) methyl)-1H-1,2,3-triazol-1-yl)ethyl)quinolin-4-Amine 21*

White solid, Yield: 83%, Mp: 132–134 °C, IR $cm^{-1}$: 3327, 3097, 2960, 2926, 2868, 1607, 1589, 1331, 1254, 1011, 871, 805; $^1H$ NMR (100 MHz, $CDCl_3$), δ: 1.18 (d, 6H, $CH_3$, $J = 7$ Hz), 2.34 (s, 3H, $CH_3$), 3.18 (sex, 1H, CH, $J = 7$ Hz), 4.00 (t, 2H, H9, $J = 6$ Hz), 4.83 (t, 2H, H10, $J = 6$ Hz), 5.24 (s, 2H, $CH_2$), 6.47 (d, 1H, H3, $J = 5$ Hz), 6.79–6.85 (m, 2H, Ar), 7.10–7.18 (m, 2H, Ar), 7.34–7.43 (m, 2H, Ar), 7.70 (s, 1H, 5H″), 7.87–8.00 (m, 2H, Ar, NH), 8.49 (brs, 1H, H2); $^{13}C$ NMR (25.8 MHz, DMSO $d_6$), δ: 21.3, 23.1, 26.5, 43.3, 48.4, 62.2, 113.6, 121.9, 124.8, 125.1, 125.5, 126.1, 133.8, 135.1, 136.3, 143.7, 150.1, 151.7, 155.8, 161.9, 169.9. (EI) m/z (%): 435.18 [M] (2), 400.15 [M-Cl] (4), 207.05 [M-$C_{13}H_{16}N_3O$] (18), 191.04 [M-$C_{14}H_{18}N_3O$] (69), 163.04 [M-$C_{13}H_{11}ClN_5$] (7), 150.09 (M-$C_{12}$H9$ClN_5$) (26), 135.07 ($C_9H_{11}O$) (100), 81.07 ($C_3H_3N_3$) (13), 67.06 ($C_2H_{11}N_3$) (18); Anal. Calcd for $C_{24}H_{26}ClN_5O$: C, 66.12; H, 6.01; N, 16.06. Found: C, 66.15; H, 6.05; N, 15.87.

#### *4.4.12 | 1-(2-((1-(2-((7-Chloroquinolin-4-yl)amino)ethyl)-1H-1,2,3-triazol-4-yl)methoxy)-4-Methoxyphenyl)ethan-1-One 22*

Beige solid, Yield: 85%, Mp: 167–168 °C, IR $cm^{-1}$: 3348, 3112, 3001, 2949, 1650, 1580, 1359, 1265, 1171, 1005, 829; $^1H$ NMR (100 MHz, $CDCl_3$), δ: 2.48 (s, 3H, $CH_3$), 3.86 (s, 3H, $OCH_3$), 3.91 (t, 2H, H9, $J = 6$ Hz), 4.76 (t, 2H, H10, $J = 6$ Hz), 5.23 (s, 2H, $CH_2$), 6.17 (brs, 1H, NH), 6.42 (d, 1H, H3, $J = 5$ Hz), 6.52 (d, 1H, H3′ $J = 2$ Hz), 6.62 (m, 2H, H5′, 6′), 7.33 (dd, 1H, H6, $J_1 = 9$ Hz, $J_2 = 2$ Hz), 7.74–7.82 (m, 2H, 5H″, H5), 7.97 (d, 1H, H8, $J = 2$ Hz), 8.53 (d, 1H, H2, $J = 5$ Hz); $^{13}C$ NMR (25.8 MHz, $CDCl_3$), δ: 31.6, 42.9, 48.8, 55.6, 62.6, 100.3, 106.2, 121.5, 121.7, 123.9, 125.8, 128.5, 132.6, 135.4, 149.2, 151.6, 164.5, 197.7; (EI) m/z (%): 408.15 [M-$C_2H_3O$] (5), 258.07 [$C_{14}H_{17}ClN_3O_2$] (16), 207.05 [M-$C_{12}H_{12}N_3O_3$] (16), 191.02 [M-$C_{13}H_{14}N_3O_3$] (70), 179.04 [M- $C_{13}H_{14}N_3O_3$] (5), 135.09 [$C_8H_7O_2$] (100), 95.02 [$C_4H_5N_3$] (9), 91.08 [$C_6H_6O$] (46); Anal. Calcd for $C_{23}H_{22}ClN_5O_3$: C, 61.13; H, 4.91; N, 15.50. Found: C, 61.13; H, 4.93; N, 15.73.

## 5 | Biology

### 5.1 | Cell Lines

The cancer cell lines used in the cytotoxic assays were acquired from the American Tissue Culture Collection (ATCC) (Manassas, VA, USA) and maintained as described previously [28]. The MRC-5 and BJ human fibroblasts were used as non-tumoral control cells. The (MRC-5 LD and BJ LD) are also human fibroblast cell lines resistant to doxorubicin. The cell line CCRF-CEM is derived from T-lymphoblastic leukemia and is highly chemosensitive. Also, the cell line K562 represents cell samples from a patient with AML that presents Bcr-Abl translocation. The Raji and Ramos cell lines are derived from B-cell leukemia. Other cells, such as U2O2, represent a pediatric osteosarcoma; HCT116 is a colorectal tumor cell line; and HCT116p53-/- (Horizon Discovery Ltd., Cambridge, UK) is a similar cell line with its p53 gene knocked down, a model of human cancer frequently associated with poor prognosis. The cells were maintained in Nunc/Corning 80 $cm^2$ plastic tissue culture flasks and cultured in a cell culture medium according to ATCC or Horizon recommendations (DMEM/RPMI 1640/McCoy with 5 g/L glucose, 2 mM glutamine, 100 U/mL penicillin, 100 mg/mL streptomycin, 10% fetal calf serum, and $NaHCO_3$).

### 5.2 | Lymphocytes from Normal Donors

Leukocytes were collected from five healthy donors at the Transfusion Medical Department of Olomouc University Hospital. The cells were isolated using the standard Ficoll–Hypaque technique, as previously outlined in relevant literature [57, 58]. Following isolation, the cells underwent a 72-h incubation period, as per the established protocol for the standard compound-screening method used at the Institute of Molecular and Translational Medicine.



18607187, 2026, 15, Downloaded from https://chemistry-europe.onlinelibrary.wiley.com/doi/10.1002/cmdc.70425 by University Palacky, Wiley Online Library on [06/08/2026]. See the Terms and Conditions (https://onlinelibrary.wiley.com/terms-and-conditions) on Wiley Online Library for rules of use; OA articles are governed by the applicable Creative Commons License

### 5.3 | Cytotoxic MTS Assay

The in vitro cytotoxicity of compounds **11**–**22** was evaluated utilizing the 3-(4,5-dimethylthiazol-2-yl)-5-(3-carboxymethoxyphenyl)-2-(sulfophenyl)-2H-tetrazolium (MTS) assay on a robotic platform (High Res BioSolutions) at the Institute of Molecular and Translational Medicine. Cell suspensions were prepared and diluted according to the specific cell type and the anticipated target cell density, which ranged from 25 000 to 35 000 cells/mL and was informed by the cells' growth characteristics as previously documented [59]. An automatic pipettor was employed to dispense 30 μL of the cell suspension into 384-well microtiter plates. All compounds under investigation were solubilized in 100% DMSO, and four-fold serial dilutions of the required test concentrations were introduced into the wells of the microtiter plates as 0.15 μL aliquots at baseline using the Echo550 echo acoustic noncontact liquid handler (Labcyte). The final DMSO concentration in the cell culture was maintained at 0.01%. The assays were performed in technical duplicates, accompanied by a minimum of three biological replicates, to enhance the reliability of the results. The cells were incubated with the tested compounds for 72 h at 37 °C in a 5% $CO_2$ atmosphere with 100% humidity.

At the conclusion of the incubation period, cell viability was assessed using the MTS assay. An aliquot of 5 μL of the MTS stock solution was added to each well, followed by incubation for 1–4 h. Subsequently, the optical density (OD) was measured at 490 nm using an Envision reader (PerkinElmer). Tumor cell survival (TCS) was calculated using the formula: TCS = (OD of drug-exposed well/mean OD of control wells) × 100%. The $IC_{50}$ value, indicative of the concentration of the compound required to achieve 50% lethality in tumor cells, was derived from the corresponding dose–response curves using Dotmatics software (updated version 2022, London, UK [60] After a period of 3 days of incubation with cancer cell lines and normal fibroblasts, the minimum inhibitory concentrations ($IC_{50}$) were determined.

### 5.4 | Spheroid Formation

Spheroid culture aims to analyze the drug's effects on complex structures that resemble solid tumors. The spheroids were prepared using the specific nonadherent plates for spheroid formation (Nunc Sphera, Thermo Fisher, Waltham, MA, USA) according to the manufacturer's simple protocol. The cell lines HCT116 parental, HCT116KOTp53, A549, and U2O2 were cultured at a density of 2500 cells per well using medium containing 10% fetal calf serum and antibiotics: McCoy's 5A medium for HCT116, F-12K (Kaighn's Modified) for A549, and Dulbecco's modified Eagle medium (DMEM). The cells were cultured for 48 h as recommended by the manufacturer and as described by Suárez et al. [60]. Spheroids were also made using BJ and MRC-5 fibroblasts, using 3000 cells per well.

### 5.5 | Spheroid Viability Assay

Cell viability of the treated spheroids was assessed using the CellTiter-Glo 3D kit (Promega Corporation, Madison, WI, USA). The kit is designed to measure ATP as an indicator of viability, generating a luminescent readout that is more sensitive than colorimetric or fluorescence-based methods. The spheroids were cultivated with compounds at concentrations ranging from 100 pM to 50 μM in triplicate for 72 h, and the luminescence was measured using the Enspire apparatus (PerkinElmer). A standard curve was performed for each analysis as recommended by the manufacturer. Cisplatin (Src tyrosine kinase inhibitor), dasatinib (BCR-ABL kinase inhibitor), sorafenib (growth factor-related tyrosine kinase inhibitor), quercetin (PKA inhibitor), and fosfatinib (Syk kinase inhibitor) were used as controls.

Morphological assessment of spheroids was performed under the inverted microscope using grids every 12 h. Only changes in spheroid size were observed during the process, which were less pronounced than the quantified ATP release.

### 5.6 | Apoptosis Quantification

Apoptosis was assessed utilizing the Human Cleaved Caspase-3 (Asp175) ELISA Kit (Abcam) on cell culture extracts obtained from each treatment group, in accordance with the manufacturer's guidelines. Absorbance was measured using an Enspire apparatus (PerkinElmer) at 450 nm.

### 5.7 | Production and Purification of the Isoform α of the Recombinant Mouse PKA Catalytic Subunit

*Escherichia coli* BL21 (DE3) cells were transformed with the pRSETB PKA Cat expression vector (Plasmid #14920, Addgene), which was kindly provided by Dr. Susan S. Taylor, University of California, San Diego, USA. pRSETB PKA Cat is a bacterial expression vector that has been engineered to contain and express the gene construct for the full-length M. musculus isoform α of the catalytic subunit of PKA (Cα). The Cα subunit was expressed in bacteria using LB medium supplemented with ampicillin (100 μg/mL). Bacterial cells were grown at 37 °C with shaking until cultures reached mid-log phase (OD600 nm = 0.6–0.7), and protein expression was initiated by adding IPTG (0.5 mM). Broth cultures were incubated overnight with shaking, and cells were harvested by centrifugation (10000×g for 30 min at 4 °C).

The Cα subunit was purified by loading the bacterial soluble fraction on a CM Sepharose Fast Flow (Sigma) column. After washing the resin thoroughly with the equilibration buffer [30 mM 2–(N-morpholino)ethanesulfonic acid, 1 mM EDTA, pH 6.5], the Cα subunit was eluted using a linear gradient of 0–0.5 M KCl in the same buffer. Two-milliliter fractions were collected, and their absorbance was measured at 280 nm. The protein's purity was analyzed by SDS-PAGE [61]. Fractions containing the pure Cα subunit were pooled, concentrated, and stored at −40 °C in the presence of 20% glycerol.

### 5.8 | Protein Kinase Activity Assay

Kinase activity of the purified recombinant PKA catalytic was determined using an electrophoretic gel-shift nonradioactive



18607187, 2026, 15, Downloaded from https://chemistry-europe.onlinelibrary.wiley.com/doi/10.1002/cmdc.70425 by University Palacky, Wiley Online Library on [06/08/2026]. See the Terms and Conditions (https://onlinelibrary.wiley.com/terms-and-conditions) on Wiley Online Library for rules of use; OA articles are governed by the applicable Creative Commons License

assay [62]. A synthetic heptapeptide known as kemptide (sequence: LRRASLG) was fluorescently labeled with fluorescamine and employed as a substrate [63]. Reaction mixtures were separated by electrophoresis on a 1% agarose gel, and the gels were visualized under a phototransilluminator using UV light.

### 5.9 | Effect of Compounds 11–22 on the Enzymatic Activity of the Cα Subunit

Kinase activity was measured following incubation of the PKA Cα subunit with various concentrations (0–10 μM) of the synthesized Click compounds dissolved in DMSO. Each experiment was performed in triplicate. Detected fluorescent bands were quantified by densitometry using ImageJ. The $IC_{50}$ (half-maximal inhibitory concentration) was determined by fitting a nonlinear regression to the normalized data using GraphPad Prism 5.0. Additionally, the purified Cα subunit was incubated with 5 mM ATP and 50 mM $MgCl_2$ prior to use to evaluate whether MgATP protected against the enzyme's inhibition by the Click compounds.

### 5.10 | Molecular Docking

Protein–ligand docking simulations were carried out using the CB-Dock2 web server (https://cadd.labshare.cn/cb-dock2/). The target protein structure was obtained from the Protein Data Bank (PDB ID: 4NTS, PDB DOI: https://doi.org/10.2210/pdb4NTS/pdb), which corresponds to the apoenzyme structure of the M. musculus PKA catalytic subunit, and the molecular structures were drawn using ChemDraw (version 23.0, PerkinElmer, Inc.). Docking was conducted by uploading the protein and ligand files to the CB-Dock2 server. The "Auto Blind Docking" option was selected to automatically detect potential binding cavities and run docking simulations.

Redocking of two cocrystallized inhibitors of the PKA Cα subunit, STU from PDB ID: 1STC and BLU0588 from PDB ID: 9PC1, was employed to validate the docking protocol. For each crystal structure, the cocrystallized ligand was extracted from the receptor, and the receptor was prepared following the same procedure adopted for the docking calculations of the synthesized compounds. The ligands were then independently redocked into the ATP-binding pocket using AutoDock Vina with the same parameters used for the synthesized compounds. The corresponding docking poses were superimposed onto their respective crystallographic conformations using PyMOL, and the RMSD between the heavy atoms of the crystallographic and redocked ligands was calculated to assess the accuracy of the docking protocol.

### 5.11 | Statistical Analysis

The Dotmatics software (Updated version 2022, London, UK) was used for the $IC_{50}$ calculations, as described previously. The different assays were analyzed using GraphPad software version 10, employing Student's t-test and one-way ANOVA [64].

#### Acknowledgments

The authors acknowledge the Instituto de Investigaciones Farmacéuticas de la Facultad de Farmacia, Universidad Central de Venezuela. This work was supported by the Ministerio de Ciencia, Tecnología e Innovación de Venezuela (grant no. 2023PGP99). All biological parts of the study were supported in part by the infrastructural projects (CZ-OPENSCREEN – LM2023052; EATRIS-CZ – LM2023053), the Czech biobank network (BBMRI - LM2023033), and the projects National Institute for Cancer Research (Program EXCELES, ID Project No. LX22NPO5102) Funded by the European Union – Next Generation EU from the Ministry of Education, Youth and Sports of the Czech Republic (MEYS), project TN02000109 (Personalized Medicine: From Translational Research into Biomedical Applications is co-financed with the state support of the Technology Agency of the Czech Republic as part of the National Centers of Competence Program).

#### Funding

This study was supported by Ministerio de Ciencia y Tecnología (Grant 2023PGP99) and National Institute for Cancer Research (Grant LX22NPO5102 and TN02000109).

#### Conflicts of Interest

The authors declare no conflicts of interest.

#### Data Availability Statement

The data that support the findings of this study are available on request from the corresponding author. The data are not publicly available due to privacy or ethical restrictions.

#### References

1. F. Bray, M. Laversanne, H. Sung, et al., "Global Cancer Statistics 2022: GLOBOCAN Estimates of Incidence and Mortality Worldwide for 36 Cancers in 185 countries," *CA: A Cancer Journal for Clinicians* 74 (2024): 229–263, https://doi.org/10.3322/caac.21834.

2. U. Anand, A. Dey, A. K. Singh Chandel, et al., "Cancer Chemotherapy and Beyond: Current Status, Drug Candidates, Associated Risks and Progress in Targeted Therapeutics," *Genes Dise* 10 (2023): 1367–1401, https://doi.org/10.1016/j.gendis 2022.

3. P. Njaria, J. Okombo, N. Njuguna, and K. Chibale, "Chloroquine-Containing Compounds: A Patent Review (2010–2014)," *Expert Opinion on Therapeutic Patents* 25 (2015): 1003–1024, https://doi.org/10.1517/13543776.2015.1050791.

4. S. Mah, J. Park, H. Jung, et al., "Identification of 4-Phenoxyquinoline Based Inhibitors for L1196M Mutant of Anaplastic Lymphoma Kinase by Structure-Based Design," *Journal of Medicinal Chemistry* 60 (2017): 9205–9221, https://doi.org/10.1021/acs.jmedchem.7b01039.

5. R. Kholiya, S. Khan, A. Bahuguna, M. Tripathi, and D. Rawat, "N-Piperonyl Substitution on Aminoquinoline-Pyrimidine Hybrids: Effect on the Antiplasmodial Potency," *European Journal of Medicinal Chemistry* 131 (2017): 126–140, https://doi.org/10.1016/j.ejmech.2017.03.007.

6. M. Joshi, J. Okombo, S. Nsumiwa, et al., "4-Aminoquinoline Antimalarials Containing a Benzylmethylpyridylmethylamine Group Are Active Against Drug Resistant *Plasmodium Falciparum* and Exhibit Oral Activity in Mice," *Journal of Medicinal Chemistry* 60 (2017): 10245–10256, https://doi.org/10.1021/acs.jmedchem.7b01537.

7. A. Mishra, H. Batchu, K. Srivastava, P. Singh, P. K. Shukla, and S. Batra, "Synthesis and Evaluation of New Diaryl ether and Quinoline Hybrids as Potential Antiplasmodial and Antimicrobial Agents," *Bioorganic &*



18607187, 2026, 15, Downloaded from https://chemistry-europe.onlinelibrary.wiley.com/doi/10.1002/cmdc.70425 by University Palacky, Wiley Online Library on [06/08/2026]. See the Terms and Conditions (https://onlinelibrary.wiley.com/terms-and-conditions) on Wiley Online Library for rules of use; OA articles are governed by the applicable Creative Commons License

*Medicinal Chemistry Letters* 24 (2014): 1719–1723, https://doi.org/10.1016/j.bmcl.2014.02.044.

8. F. Smit and D. N'Da, "Synthesis, In Vitro Antimalarial Activity and Cytotoxicity of Novel 4-Aminoquinolinyl-Chalcone Amides," *Bioorganic & Medicinal Chemistry* 22 (2014): 1128–1138, https://doi.org/10.1016/j.bmc.2013.12.032.

9. Md Mushtaque and Shahjahan, "Reemergence of Chloroquine (CQ) Analogs as Multi-Targeting Antimalarial Agents: A Review," *European Journal of Medicinal Chemistry* 90 (2015): 280–295, https://doi.org/10.1016/j.ejmech.2014.11.022.

10. D. Kumar, S. Khan, B. Tekwani, P. Ponnan, and D. Rawat, "4-Aminoquinoline-Pyrimidine Hybrids: Synthesis, Antimalarial Activity, Heme Binding and Docking Studies," *European Journal of Medicinal Chemistry* 89 (2015): 490–502, https://doi.org/10.1016/j.ejmech.2014.10.061.

11. R. Raj, J. Gut, P. Rosenthal, and V. Kumar, "1H-1,2,3-Triazole-Tethered Isatin-7-Chloroquinoline and 3-Hydroxy-Indole-7-Chloroquinoline Conjugates: Synthesis and Antimalarial Evaluation," *Bioorganic & Medicinal Chemistry Letters* 24 (2014): 756–759, https://doi.org/10.1016/j.bmcl.2013.12.109.

12. B. S. Matada, R. Pattanashettar, and N. G. Yernale, "A Comprehensive Review on the Biological Interest of Quinoline and Its Derivatives," *Bioorganic & Medicinal Chemistry* 32 (2021): 115973, https://doi.org/10.1016/j.bmc.2020.115973.

13. C. F. M. Silva, D. C. G. A. Pinto, P. A. Fernandes, and A. M. S. Silva, "Evolution of the Quinoline Scaffold for the Treatment of Leishmaniasis: A Structural Perspective," *Pharmaceuticals* 17 (2024): 285, https://doi.org/10.3390/ph17030285.

14. L. Monzote, L. Machín, A. González, et al., "Eugenol-Rich Essential Oil From *Pimenta dioica*: In Vitro and In Vivo Potentialities Against *Leishmania amazonensis*," *Pharmaceuticals* 17 (2024): 64, https://doi.org/10.3390/ph17010064.

15. L. P. R. Figueroa, N. A. dos Santos, P. H. O. Santiago, et al., "Synthesis and Evaluation of Antibacterial Activity of 1,2,3-Triazole and ether Derivatives of Paeonol," *Journal of the Brazilian Chemical Society* 34 (2023): 25–35, https://doi.org/10.21577/0103-5053.20220085.

16. S. S. Arya, J. E. Rookes, D. M. Cahill, and S. K. Lenka, "Vanillin: A Review on the Therapeutic Prospects of a Popular Flavouring Molecule," *Advances in Traditional Medicine* 21 (2021): 415–431, https://doi.org/10.1007/s13596-020-00531-w.

17. A. Escobar, M. Pérez, G. Romanelli, and G. Blustein, "Thymol Bioactivity: A Review Focusing on Practical Applications," *Arabian Journal of Chemistry* 13 (2020): 9243–9269, https://doi.org/10.1016/j.arabjc.2020.11.009.

18. D. P. Vala, R. M. Vala, and H. M. Patel, "Versatile Synthetic Platform for 1,2,3-Triazole Chemistry," *ACS Omega* 7 (2022): 36945–36987, https://doi.org/10.1021/acsomega.2c04883.

19. M. J. Vaishnani, S. Bijani, M. Rahamathulla, et al., "Biological Importance and Synthesis of 1,2,3-Triazole Derivatives: A Review," *Green Chemistry Letters and Reviews* 17 (2024): 2307989, https://doi.org/10.1080/17518253.2024.2307989.

20. K. S. Bhullar, N. O. Lagarón, E. M. McGowan, et al., "Kinase-Targeted Cancer Therapies: Progress, Challenges and Future Directions," *Molecular Cancer* 17 (2018): 48, https://doi.org/10.1186/s12943-018-0804-2.

21. K. J. Rosenthal, J. D. Gordan, and J. D. Scott, "Protein Kinase a and Local Signaling in Cancer," *The Biochemical Journal* 48 (2024): 1659–1677, https://doi.org/10.1042/BCJ20230352.

22. L. Sapio, F. Di Maiolo, M. Illiano, et al., "Targeting Protein Kinase a in Cancer Therapy: An Update," *EXCLI Journal* 13 (2014): 843–855.

23. Y. S. Cho, Y. N. Lee, and Y. S. Cho-Chung, "Biochemical Characterization of Extracellular cAMP-Dependent Protein Kinase as a Tumor Marker," *Biochemical and Biophysical Research Communications* 278 (2000): 679–684, https://doi.org/10.1006/bbrc.2000.3853.

24. M. E. Cvijic, T. Kita, W. Shih, R. S. DiPaola, and K. V. Chin, "Extracellular Catalytic Subunit Activity of the cAMP-Dependent Protein Kinase in Prostate Cancer," *Clinical Cancer Research* 6 (2000): 2309–2317.

25. Y. Wu, Y. Li, J. Liu, et al., "The Diagnostic Value of Extracellular Protein Kinase a (ECPKA) in Serum for Gastric and Colorectal Cancer," *Translational Cancer Research* 9 (2020): 3870–3878, https://doi.org/10.21037/tcr-20-764.

26. H. Zhang, Y. Liu, J. Liu, et al., "cAMP-PKA/EPAC Signaling and Cancer: The Interplay in Tumor Microenvironment," *Journal of Hematology & Oncology* 17 (2024): 5, https://doi.org/10.1186/s13045-024-01524-x.

27. S. Naviglio, M. Caraglia, A. Abbruzzese, et al., "Protein Kinase a as a Biological Target in Cancer Therapy," *Expert Opinion on Therapeutic Targets* 13 (2009): 83–92, https://doi.org/10.1517/14728220802602349.

28. J. E. Gutiérrez, H. Ramírez, E. Fernandez-Moreira, et al., "Synthesis, Antimalarial, Antileishmanial, and Cytotoxicity Activities and Preliminary in Silico ADMET Studies of 2-(7-Chloroquinolin-4-Ylamino)ethyl Benzoate Derivatives," *Pharmaceuticals* 16 (2023): 1709, https://doi.org/10.3390/ph16121709.

29. A. Mijoba, N. Parra-Giménez, E. Fernandez-Moreira, et al., "Synthesis of Hybrid Molecules With Imidazole-1,3,4-Thiadiazole Core and Evaluation of Biological Activity on *Trypanosoma Cruzi* and *Leishmania Donovani*," *Molecules* 29 (2024): 4125, https://doi.org/10.3390/molecules29174125.

30. M. A. Rodríguez, A. Mijoba, N. J. Parra-Giménez, et al., "Synthesis, Evaluation of the Biological Activity Against *Trypanosoma cruzi* and *Leishmania donovani*. Preliminary in Silico ADMET Studies of 5-Nitroimidazole Derivatives," *European Journal of Medicinal Chemistry Reports* 13 (2025): 100248, https://doi.org/10.1016/j.ejmcr.2025.100248.

31. V. V. Rostovtsev, L. G. Green, V. V. Fokin, and K. B. Sharpless, "A Stepwise Huisgen Cycloaddition Process: Copper(I)-Catalyzed Regioselective 'Ligation' of Azides and Terminal Alkynes," *Angewandte Chemie International Edition* 41 (2002): 2596–2599, https://doi.org/10.1002/1521-3773(20020715)41:143.0.CO;2-4.

32. D. R. Knighton, J. H. Zheng, L. F. Ten Eyck, et al., "Crystal Structure of the Catalytic Subunit of Cyclic Adenosine Monophosphate-Dependent Protein Kinase," *Science* 253 (1991): 407–414, https://doi.org/10.1126/science.1862342.

33. D. R. Knighton, J. H. Zheng, L. F. Ten Eyck, N. H. Xuong, S. S. Taylor, and J. M. Sowadski, "Structure of a Peptide Inhibitor Bound to the Catalytic Subunit of Cyclic Adenosine Monophosphate-Dependent Protein Kinase," *Science* (1991): 414–420, https://doi.org/10.1126/science.1862343.

34. A. Y. Kovalevsky, H. Johnson, B. L. Hanson, et al., "Low- and Room-Temperature X-Ray Structures of Protein Kinase a Ternary Complexes Shed New Light on Its Activity," *Acta Crystallographica Section D Biological Crystallography* D68 (2012): 854–860, https://doi.org/10.1107/S0907444912014886.

35. C. Bissantz, B. Kuhn, and M. Stahl, "A Medicinal Chemist's Guide to Molecular Interactions," *Journal of Medicinal Chemistry* 53 (2010): 5061–5084, https://doi.org/10.1021/jm100112j.

36. L. Prade, R. A. Engh, A. Girod, V. Kinzel, R. Huber, and D. Bossemeyer, "Staurosporine-Induced Conformational Changes of cAMP-Dependent Protein Kinase Catalytic Subunit Explain Inhibitory Potential," *Structure* 5 (1997): 1627–1637, https://doi.org/10.1016/s0969-2126(97)00310-9.

37. J. G. H. Bruystens, J. Wu, G. Tan, et al., "A PKA-Selective Inhibitor Captures an Open but More Ordered Conformation of the PKA Catalytic Subunit," *Proceedings of the National Academy of Sciences of the United*



18607187, 2026, 15, Downloaded from https://chemistry-europe.onlinelibrary.wiley.com/doi/10.1002/cmdc.70425 by University Palacky, Wiley Online Library on [06/08/2026]. See the Terms and Conditions (https://onlinelibrary.wiley.com/terms-and-conditions) on Wiley Online Library for rules of use; OA articles are governed by the applicable Creative Commons License

*States of America* 123 (2026): e2536312123, https://doi.org/10.1073/pnas.2536312123.

38. K. Mena-Ulecia, W. Tiznado, and J. Caballero, "Study of the Differential Activity of Thrombin Inhibitors Using Docking, QSAR, Molecular Dynamics, and MM-GBSA," *PLoS One* 10 (2015): e0142774, https://doi.org/10.1371/journal.pone.0142774.

39. N. Dayal, E. Řezníčková, D. E. Hernandez, et al., "3H-Pyrazolo[4,3-f] quinoline-Based Kinase Inhibitors Inhibit the Proliferation of Acute Myeloid Leukemia Cells In Vivo," *Journal of Medicinal Chemistry* 64 (2021): 10981–10996, https://doi.org/10.1021/acs.jmedchem.1c00330.

40. J. P. Hughes, S. Rees, S. B. Kalindjian, and K. L. Philpott, "Principles of Early Drug Discovery," *British Journal of Pharmacology* 162 (2011): 1239–1249, https://doi.org/10.1111/j.1476-5381.2010.01127.x.

41. J. A. Arnott and S. L. Planey, "The Influence of Lipophilicity in Drug Discovery and Design," *Expert Opinion on Drug Discovery* 7 (2012): 863–875, https://doi.org/10.1517/17460441.2012.714363.

42. P. A. Insel, L. Zhang, F. Murray, H. Yokouchi, and A. C. Zambon, "Cyclic AMP Is Both a pro-Apoptotic and Anti-Apoptotic Second Messenger," *Acta Physiologica (Oxford)* 204 (2012): 277–287, https://doi.org/10.1111/j.1748-1716.2011.02273.x.

43. Z. A. Knight and K. M. Shokat, "Features of Selective Kinase Inhibitors," *Chemistry & Biology* 12 (2005): 621–637, https://doi.org/10.1016/j.chembiol.2005.04.011.

44. A. L. Hopkins, "Network Pharmacology: The Next Paradigm in Drug Discovery," *Nature Chemical Biology* 4 (2008): 682–690, https://doi.org/10.1038/nchembio.118.

45. W. Hemmer, M. McGlone, I. Tsigelny, and S. S. Taylor, "Role of the Glycine Triad in the ATP-Binding Site of cAMP-Dependent Protein Kinase," *The Journal of Biological Chemistry* 272 (1997): 16946–16954, https://doi.org/10.1074/jbc.272.27.

46. A. C. Dar and K. M. Shokat, "The Evolution of Protein Kinase Inhibitors From Antagonists to Agonists of Cellular Signaling," *Annual Review of Biochemistry* 80 (2011): 769–795, https://doi.org/10.1146/annurev-biochem-090308-173656.

47. L. M. Graves, J. S. Duncan, M. C. Whittle, and G. L. Johnson, "The Dynamic Nature of the Kinome," *The Biochemical Journal* 450, no. 1 (2013): 1-8, https://doi.org/10.1042/BJ20121456.

48. P. Zhang, F. A. Solari, J. W. M. Heemskerk, et al., "Differential Regulation of GPVI-Induced Btk and Syk Activation by PKC, PKA and PP2a in Human Platelets," *IMJS* 24 (2023): 7776, https://doi.org/10.3390/ijms24097776.

49. L. Wu, M. Yu, H. Liang, et al., "SJB2-043, a USP1 Inhibitor, Suppresses A549 Cell Proliferation, Migration, and EMT via Modulation of PI3K/AKT/mTOR, MAPK, and Wnt Signaling Pathways," *Current Issues in Molecular Biology* 47 (2025): 155, https://doi.org/10.3390/cimb47030155.

50. J. Liang, Y. Pan, J. Yang, D. Zeng, and J. Li, "WNT Signaling in Cancer: Molecular Mechanisms and Potential Therapies," *Molecular Biomedicine* 6 (2025): 83, https://doi.org/10.1186/s43556-025-00327-x.

51. M. Irfan, B. Aneja, U. Yadava, et al., "Synthesis, QSAR and Anticandidal Evaluation of 1,2,3-Triazoles Derived From Naturally Bioactive Scaffolds," *European Journal of Medicinal Chemistry* 93 (2015): 246–254, https://doi.org/10.1016/j.ejmech.2015.02.007.

52. E. M. Guantai, K. Ncokazi, T. J. Egan, et al., "Design, Synthesis and In Vitro Antimalarial Evaluation of Triazole-Linked Chalcone and Dienone Hybrid Compounds," *Bioorganic & Medicinal Chemistry* 18 (2010): 8243–8256, https://doi.org/10.1016/j.bmc.2010.10.009.

53. L. Krstulovic, K. Miškovic Špoljaric, V. Rastija, N. Filipovic, M. Bajic, and L. Glavaš-Obrovac, "Novel 1,2,3-Triazole-Containing Quinoline–Benzimidazole Hybrids: Synthesis, Antiproliferative Activity Silico ADME Predictions, and Docking," *Molecules* 28 (2023): 6950, https://doi.org/10.3390/molecules28196950.

54. B. Aneja, M. Azam, S. Alam, et al., "Natural Product-Based 1,2,3-Triazole/Sulfonate Analogues as Potential Chemotherapeutic Agents for Bacterial Infections," *ACS Omega* 3 (2018): 6912–6930, https://dx.doi.org/10.1021/acsomega.8b00582.

55. M. Pal, K. Parasuraman, and K. R. Yeleswarapu, "Palladium-Catalyzed Cleavage of O/N-Propargyl Protecting Groups in Aqueous Media Under a Copper-Free Condition," *Organic Letters* 5 (2003): 349–352, https://doi.org/10.1021/ol027382t.

56. M. V. N. de Souza, K. C. Pais, C. R. Kaiser, M. A. Peralta, M. de L. Ferreira, and M. C. S. Lourenço, "Synthesis and In Vitro Antitubercular Activity of a Series of Quinoline Derivatives," *Bioorganic & Medicinal Chemistry* 17 (2009): 1474–1480, https://doi.org/10.1016/j.bmc.2009.01.013.

57. G. P. Martínez, M. R. Mijares, K. Chávez, et al., "Caracasine Acid, an Ent-3,4-Seco-Kaurene, Promotes Apoptosis and Cell Differentiation Through NFkB Signal Pathway Inhibition in Leukemia Cells," *European Journal of Pharmacology* 862 (2019): 172624, https://doi.org/10.1016/j.ejphar.2019.172624.

58. G. P. Martínez, M. R. Mijares, K. Chávez, P. Chirinos, A. I. Suárez, and J. B. De Sanctis, "Caracasine, an Ent-Kaurane Diterpene With Proapoptotic and pro-Differentiator Activity in Human Leukemia Cell Lines," *Anti-Cancer Agents in Medicinal Chemistry* 23 (2023): 1145–1155, https://doi.org/10.2174/1871520622666220415105615.

59. J. E. Gutiérrez, E. Fernandez-Moreira, M. A. Rodríguez, et al., "Novel 7-Chloro-(4-Thioalkylquinoline) Derivatives: Synthesis and Antiproliferative Activity Through Inducing Apoptosis and DNA/RNA Damage," *Pharmaceuticals* 15 (2022): 1234, https://doi.org/10.3390/ph15101234.

60. A. I. Suárez, K. Chávez, J. V. Garmendia, et al., "New Derivatives of Caracasine Acid With Anti-Leukemic Activity and Limited Effectiveness in Spheroid Cultures," *Pharmaceuticals* 18 (2025): 1043, https://doi.org/10.3390/ph18071043.

61. U. K. Laemmli, "Cleavage of Structural Proteins During the Assembly of the Head of Bacteriophage T4," *Nature* 227 (1970): 680–685, https://doi.org/10.1038/227680a0.

62. A. Guevara, C. Lugo, A. J. Montilla, N. A. Araujo, M. Calabokis, and J. Bubis, "Glucose Deprivation Activates a cAMP-Independent Protein Kinase From *Trypanosoma Equiperdum*," *Parasitology* 146 (2019): 643–652, https://doi.org/10.1017/S0031182018001920.

63. N. A. Araujo, A. Guevara, M. A. Lorenzo, M. Calabokis, and J. Bubis, "Fluram-Kemptide-lys8 Non-Radioactive Assay for Protein Kinase a," *The Protein Journal* 35 (2016): 247–255, https://doi.org/10.1007/s10930-016-9667-9.

64. N. K. Rampeesa, R. Gundla, G. Muddasami, et al., "Identification of a Novel Azaspirooxindolinone-Based PROTACs for Selective BTK Degradation and Enhanced Anticancer Activity," *Bioorganic Chemistry* 157 (2025): 108316, https://doi.org/10.1016/j.biooSrg.2025.108316.

## Supporting Information

Additional supporting information can be found online in the Supporting Information section.



18607187, 2026, 15, Downloaded from https://chemistry-europe.onlinelibrary.wiley.com/doi/10.1002/cmdc.70425 by University Palacky, Wiley Online Library on [06/08/2026]. See the Terms and Conditions (https://onlinelibrary.wiley.com/terms-and-conditions) on Wiley Online Library for rules of use; OA articles are governed by the applicable Creative Commons License